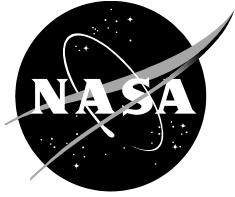# Mid-Fidelity Computational Fluid Dynamics Analysis of the Elytron 4S UAV Concept

Witold J. F. Koning
Science and Technology Corporation, Moffett Field, California

Carl Russell
Ames Research Center, Moffett Field, California

Eduardo Solis
Science and Technology Corporation, Moffett Field, California

Colin Theodore
Ames Research Center, Moffett Field, California

November 2018

NASA STI Program ... in Profile

Since its founding, NASA has been dedicated to the advancement of aeronautics and space science. The NASA scientific and technical information (STI) program plays a key part in helping NASA maintain this important role.

The NASA STI program operates under the auspices of the Agency Chief Information Officer. It collects, organizes, provides for archiving, and disseminates NASA's STI. The NASA STI program provides access to the NTRS Registered and its public interface, the NASA Technical Reports Server, thus providing one of the largest collections of aeronautical and space science STI in the world. Results are published in both non-NASA channels and by NASA in the NASA STI Report Series, which includes the following report types:

- TECHNICAL PUBLICATION. Reports of completed research or a major significant phase of research that present the results of NASA Programs and include extensive data or theoretical analysis. Includes compilations of significant scientific and technical data and information deemed to be of continuing reference value. NASA counterpart of peer-reviewed formal professional papers but has less stringent limitations on manuscript length and extent of graphic presentations.

- TECHNICAL MEMORANDUM. Scientific and technical findings that are preliminary or of specialized interest, e.g., quick release reports, working papers, and bibliographies that contain minimal annotation. Does not contain extensive analysis.

- CONTRACTOR REPORT. Scientific and technical findings by NASA-sponsored contractors and grantees.

- CONFERENCE PUBLICATION. Collected papers from scientific and technical conferences, symposia, seminars, or other meetings sponsored or co-sponsored by NASA.

- SPECIAL PUBLICATION. Scientific, technical, or historical information from NASA programs, projects, and missions, often concerned with subjects having substantial public interest.

- TECHNICAL TRANSLATION. English-language translations of foreign scientific and technical material pertinent to NASA's mission.

Specialized services also include organizing and publishing research results, distributing specialized research announcements and feeds, providing information desk and personal search support, and enabling data exchange services.

For more information about the NASA STI program, see the following:

- Access the NASA STI program home page at http://www.sti.nasa.gov

- E-mail your question to help@sti.nasa.gov

- Phone the NASA STI Information Desk at 757-864-9658

- Write to:
  NASA STI Information Desk
  Mail Stop 148
  NASA Langley Research Center
  Hampton, VA 23681-2199

NASA/TM—2018–219788
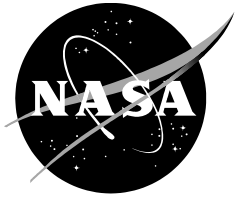
Mid-Fidelity Computational Fluid Dynamics Analysis of the Elytron 4S UAV Concept

Witold J. F. Koning
Science and Technology Corporation, Moffett Field, California

Carl Russell
Ames Research Center, Moffett Field, California

Eduardo Solis
Science and Technology Corporation, Moffett Field, California

Colin Theodore
Ames Research Center, Moffett Field, California

National Aeronautics and
Space Administration

Ames Research Center
Moffett Field, CA 94035-1000

November 2018

Acknowledgments

Available from:

Table of Contents

List of Figures

List of Tables

Nomenclature

a	distance of new CG location from origin along z
A_{global}	dimension of a boundary or global cell
a_{ng}	global refinement level
a_{rl}	cell size corresponding to refinement level
b	distance of new CG location from origin along x
c	distance between origin and rotor thrust vector along y
D	drag, positive downstream, parallel to freestream
F_D	drag force
F_L	lift force
F_S	side force
F_{T_L}	rotor thrust (left)
F_{T_R}	rotor thrust (right)
F_{x_b}	body force along x-axis
F_{y_b}	body force along y-axis
F_{z_b}	body force along z-axis
k	turbulence kinetic energy (in k-ε turbulence model)
L	lift, positive "up," normal to freestream
M	Mach number
M_{Q_L}	rotor torque (left)
M_{Q_R}	rotor torque (right)
M_x	total moment around body x-axis
M_{x_b}	moment due to aerodynamic forces on body (excluding rotor forces) around x-axis
M_y	total moment around body y-axis
M_{y_b}	moment due to aerodynamic forces on body (excluding rotor forces) around y-axis
M_z	total moment around body z-axis
M_{z_b}	moment due to aerodynamic forces on body (excluding rotor forces) around z-axis
n_{rl}	refinement level at which the cell size is to be approximated
r	rotor radial coordinate
R	rotor radius
Re	Reynolds number, $Re = \rho V L/\mu$
S	side force, positive right, looking forward
T	thrust; time
ts	time step
V	free-stream velocity
x	body-fixed axis, positive "upstream"; Cartesian x-axis
y	body-fixed axis, positive right, looking forward; Cartesian y-axis
z	body-fixed axis, positive "down"; Cartesian z-axis
α	angle of attack
β	angle of sideslip
ε	dissipation of turbulence energy (in k-ε turbulence model)
θ	pitch, positive nose up
μ	arithmetic mean
ϕ	roll, positive right wing down
ψ	yaw, positive nose right

4S	Four-Seater
ABR	Automated Body Refinement
ADM	Actuator-Disk Model
BEM	Blade-Element Model
CAD	Computer Aided Design
CFD	Computational Fluid Dynamics
CG	Center of Gravity
CPU	Central Processing Unit
CTOL	Conventional Takeoff and Landing
DELIVER	Design Environment for Novel Vertical Lift Vehicles
FOD	Foreign Object Debris
GDDR	Graphics Double Data Rate
GPS	Global Position System
GPU	Graphics Processing Unit
IGE	In Ground Effect
ISA	International Standard Atmosphere
NURBS	Non-Uniform Rational Basis Spline
RAM	Random Access Memory
RotCFD	Rotorcraft CFD
RPM	Revolutions Per Minute
STL	CAD file format
UAV	Unmanned Aerial Vehicle
URANS	Unsteady Reynolds-Averaged Navier-Stokes
UV	Ultraviolet
VTOL	Vertical Takeoff and Landing

Mid-Fidelity Computational Fluid Dynamics Analysis of the Elytron 4S UAV Concept

Witold J. F. Koning,[†] Carl Russell, Eduardo Solis,[†] and Colin Theodore

Ames Research Center

Summary

The Elytron 4S Unmanned Aerial Vehicle (UAV) Concept was developed to combine the advantages of fixed- and rotary-wing technology. The 4S Concept is a box-wing configuration with rotors mounted on a centrally located tiltwing. The UAV is intended to be capable of both conventional takeoff and landing (CTOL) and vertical takeoff and landing (VTOL), and is envisioned to excel in UAV performance because of the combined efficiency of fixed-wing aircraft and the hover and VTOL capabilities of regular drones or quadcopters.

A mid-fidelity Unsteady Reynolds-Averaged Navier-Stokes (URANS) approach using Rotorcraft CFD (RotCFD) is performed to analyze and characterize the performance of the aircraft. The flow field is coupled with a rotor model based on blade-element momentum theory to model the 4S UAV rotors. Turbulence is modeled using a realizable k-ε turbulence model with special wall function. The code is used to generate aerodynamic forces and moments on the body at cruise conditions, and during VTOL. The results and their uncertainties are characterized, and an angle-of-attack and sideslip sweep are computed, both with and without rotors on.

Simulations are compared with the wind tunnel tests in the 7- by 10-Foot U.S. Army Wind Tunnel at NASA Ames Research Center, performed in 2017. Results show promising comparison with experimental data, despite a late change in rotor size and rudder size of the physical model that cause the expected deviations from the simulation. A slight change in the net thrust value, when rotors are modeled, is observed because of the rotor diameter increase on the physical model. A noticeable difference in the directional stability was observed because of the increased rudder surface and added strakes. These changes were implemented to improve on the design as simulated, which is observed in the results. The simulation results paved the way to the first successful flight of the UAV Concept.

Introduction

Advances in electric motor technology, battery technology, and electronics have dramatically increased the capabilities of Unmanned Aerial Vehicles (UAVs) in recent years. The Elytron 4S UAV Concept was developed to combine the advantages of both fixed- and rotary-wing technology, by utilizing a box-wing configuration with rotors mounted on a centrally located tiltwing.

The present work provides a mid-fidelity computational fluid dynamics (CFD) analysis of the 4S UAV Concept using Rotorcraft CFD (RotCFD) to indicate regions of potential improvement for the design. The code is used to generate aerodynamic forces and moments on the body at cruise

---

[†] Science and Technology Corporation, NASA Research Park, Moffett Field, CA 94035.

conditions, and during vertical takeoff and landing (VTOL). Simulations are compared with the wind tunnel tests in the 7- by 10-Foot U.S. Army Wind Tunnel at NASA Ames Research Center, performed in 2017. The work is performed during the developmental phase of the Elytron 4S UAV to provide both a performance estimate of the UAV, and to investigate the accuracy of the mid-fidelity methods used for performance estimates of UAVs in this low-speed regime.

Elytron 4S Concept

The Elytron 4S UAV Concept is an aircraft derived from a family of "Elytron" concept designs all based on a similar box-wing configuration with a dual propeller/rotor tiltwing. The tiltwing allows the aircraft to operate in VTOL and aircraft mode, thereby allowing for a design that can take off vertically but can achieve efficiencies in forward flight resembling a fixed-wing aircraft. Figure 1 shows a Computer Aided Design (CAD) rendering of the Elytron 4S Concept. The designation "4S" stands for four-seater.

Figure 1. CAD rendering of Elytron 4S (full-scale) conceptual design.

4S UAV Concept

The 4S UAV Concept was developed to learn more about the flight dynamics of the design by building a small-scale model. It also serves to identify the concept's potential use as a small UAV for Earth observation or small cargo transport.

The 4S UAV is a small-scale replica of the full-scale vehicle, with modifications. The propellers are three-bladed, and the vertical wings (excluding the tail) are flat sheets instead of profiled airfoils. The model is powered by a lithium-polymer battery and is equipped with motors capable of powered vertical takeoff. The aircraft is equipped with a range of sensors and radios to allow for remote control and logging of telemetry. The 4S UAV Concept also utilizes a nose fan for pitch control in VTOL operation, as the rotors lack collective and cyclic control. The Elytron 4S UAV is intended to have closed-loop attitude control and stabilization.

4S UAV Tunnel Model

The physical model tested in the 7- by 10-Foot U.S. Army Wind Tunnel at NASA Ames Research Center is a carbon fiber replica of the CAD model, as shown in Figure 2. Because the model is a one-off, hand-built model, there are some minor differences compared to the CAD. The "winglets" are slightly bent instead of straight flat plates, and some surface roughness is present in the finishing of the surface on the model. Furthermore, some antennae are present

2

(Global Position System (GPS) antenna, and smaller telemetry antennas) that are not included in the CAD model. The cutout for the motors in the leading edge of the tiltwing is not modeled in CAD, and some tufts are applied on the right side of the model (see Figure 3).

Prior to tunnel testing, the rudder length and rotor size were slightly increased and strakes were added to the Elytron model. Because of changes in the design, a slight change in the net thrust value is expected when rotors are modeled. A noticeable change in directional stability is also expected because of the increased rudder surface and added strakes.

For the "rotors-off" tests, the nose fan was covered over, and the propellers were removed. Figure 3 and Figure 4 show protruding antennae, motor cutout, tuft (dots), and exposed cabling. The black dots (shown enlarged in Figure 5) are the glue holding the fluorescent micro tufts in place.

Figure 2. Elytron 4S UAV in 7- by 10-Foot U.S. Army Wind Tunnel at NASA Ames Research Center (2017).

Figure 3. Close-up of Elytron 4S UAV protruding antennae, motor cutout, tuft (dots), and exposed cabling.
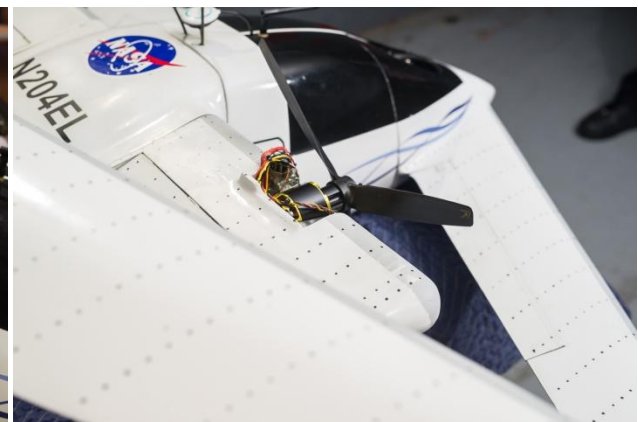
Figure 4. Elytron 4S UAV motor cutout, tuft (dots), and exposed cabling.
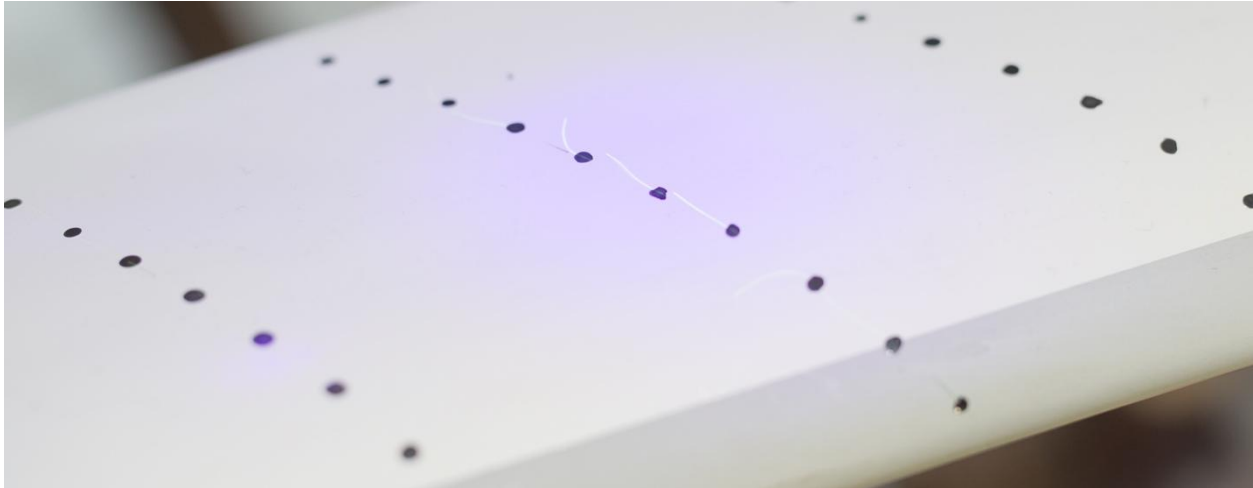
Figure 5. Elytron 4S UAV tuft dots and fluorescent micro tufts light up under an ultraviolet (UV) light.

4S UAV CFD Model

The reverse engineering process uses specialized measuring tools and CAD software to generate the CFD grids of the Elytron fuselage and rotor blades for RotCFD analysis. The CFD grid for the Elytron 4S was reconstructed in Rhino 5.0[‡] using the non-watertight geometry in .STL format (polygonal mesh) provided by the manufacturer. The STL geometry was divided into several sections in order to rebuild the geometry using nonuniform rational basis spline (NURBS) surfaces. The NURBS surface 3D model was used to generate two configurations; airplane mode (Figure 6) and helicopter mode (Figure 7). The global origin of the aircraft was relocated between the rotor blades in line with the quarter chord of the tilting wing (pivot axis).

Discrete surface measurements of the rotor and ducted fan were acquired using a 3D optical laser scanner called the Creaform MetraScan 70.[§] The laser power and resolution were maximized to resolve the rough black matte finish and thin trailing edges. The point clouds were converted to polygonal meshes processed in PolyWorks.[**] In PolyWorks Modeler, the wireframe to rebuild the rotor blade surfaces is composed of cross sections and profile curves manually fitted to the point cloud (see Figure 8). The curves are then verified by automatically generating NURBS patches that are fitted to the curves and the point cloud as shown in Figure 9. The same methodology was performed on the ducted fan.
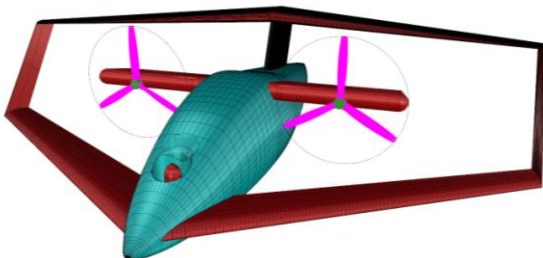
Figure 6. NURBS surface model in airplane mode.
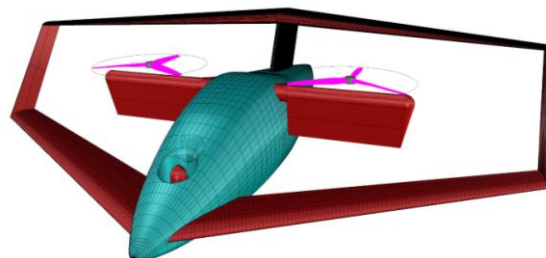
Figure 7. NURBS surface model in helicopter mode.

[‡] https://www.rhino3d.com/

[§] https://www.creaform3d.com/

[**] https://www.innovmetric.com/
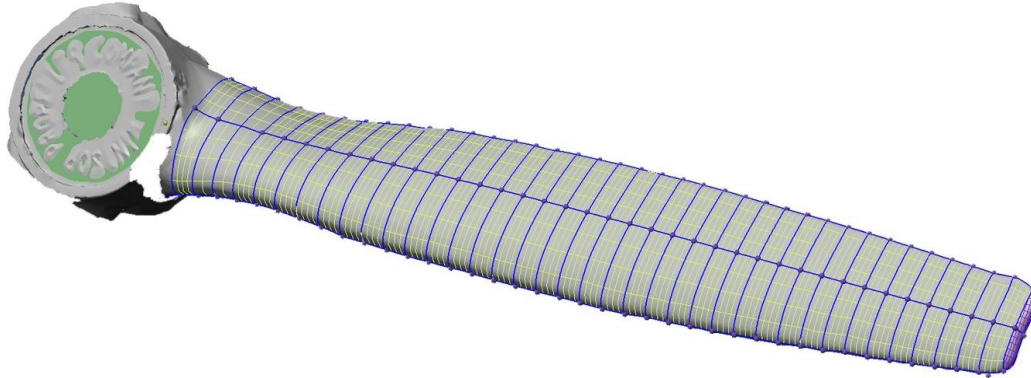
Figure 8. Rotor blade geometry with polygonal model shown in gray, cross-section and profile curves shown in blue, and NURBS patches shown in green.
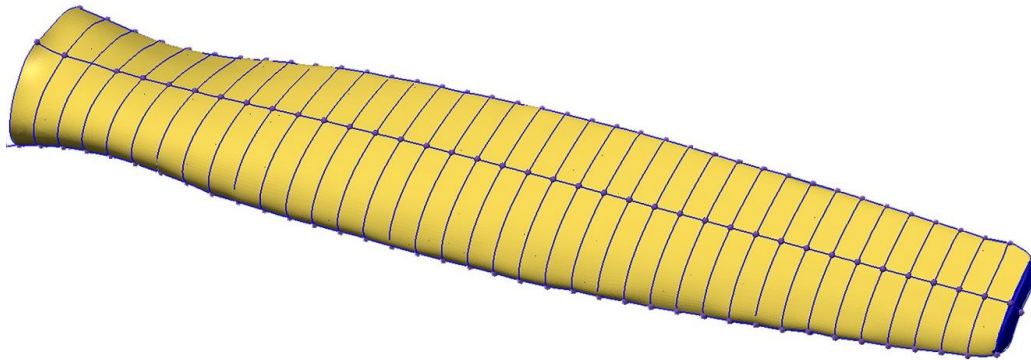
Figure 9. Rotor blade geometry with NURBS patches converted to NURBS surfaces as shown in yellow.

The NURBS surfaces are imported into Rhino 5.0 to finalize the geometry and generate the airfoil cross sections for CFD analysis. Figure 10 shows the watertight rotor blade and extracted cross sections as equally segmented points. The same methodology was performed on the ducted fan, shown in Figure 11.
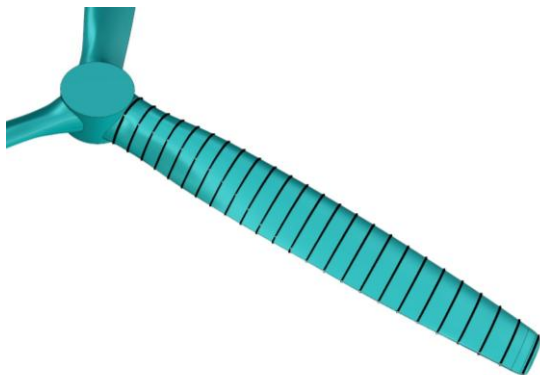
Figure 10. 14-inch-diameter rotor blade; 25 cross sections made up of equally segmented points were extracted at specified radial stations.
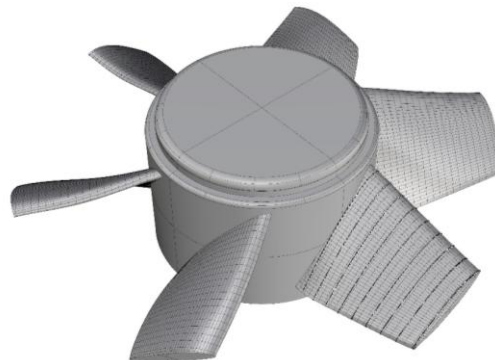
Figure 11. Ducted fan; nine cross sections made up of equally segmented points were extracted at specified radial stations.

Rotorcraft CFD: RotCFD

The mid-fidelity CFD software RotCFD [1] is used to perform the analysis of the rotor's performance and the complete airframe. RotCFD models the rotor through a momentum source approach using a blade-element model (BEM) or actuator-disk model (ADM), which utilizes an airfoil deck (C81) as input. The present work uses only the BEM rotor modeling technique for the main rotors, to increase the fidelity of the rotor (and subsequent rotor wake) modeling. The rotor flow field and subsequent performance is then modeled in an Unsteady Reynolds-Averaged Navier-Stokes (URANS) flow field through the momentum that the rotor model imparts on the flow. The flow field does not have a rotor geometry embedded within the grid; it only observes the effects of the rotor's presence superimposed on the corresponding cells in the flow field. This method allows for good performance measurements of rotors, while also allowing for interactions with airframes [2], [3]. RotCFD uses a realizable k-ε turbulence model with special wall function. No transition model or trip methods are available to control transition to turbulent flow at the time of writing. RotCFD can incorporate bodies—mostly to investigate download of the rotor on the body—but is not intended specifically to simulate lifting bodies; the gridding options are not adequate enough to correctly capture the boundary layer, making accurate aerodynamic forces hard to obtain.

RotUNS is a submodule of RotCFD using an unstructured grid with the possibility of simulating multiple rotors and bodies in the flow field. RotUNS is used for all simulations unless otherwise noted. RotUNS uses an unstructured Cartesian grid in the far field with a tetrahedral near-body grid for body fitting. This research must not be interpreted as a high-fidelity simulation; rather, the objective is to see how well general trends can be captured with mid-fidelity models and quick turnaround times.

Parallel Computing and Limitations

Since the introduction of RotCFD version r400, parallel processing using a single graphics processing unit (GPU) is possible, achieving a reduction in wall clock time for simulations of around an order of magnitude.[††] The goal of RotCFD is to be able to run on "normal- to workstation-class PCs." The intent to parallelize computations on a cluster of multiple PCs is therefore not within the scope. However, a GPU is a much used and inexpensive way of parallel processing. Previous RotCFD versions allowed running only on the central processing unit (CPU) either in Serial (single core) or OpenMP mode (multiple cores). The addition of parallel processing on the GPU allows for running in OpenCL.

The GPUs used for this effort are relatively low-power NVIDIA GeForce GTX 750 Ti's with 2GB of graphics double data rate (GDDR) memory. In OpenCL mode, RotCFD can use the computer's main random access memory (RAM), but in OpenCL the GPUs' on-board video RAM is a limiting factor. This quickly translates into a maximum cell count for the simulation. For the GeForce GTX 750 Ti's used in the present work, that limit is around 1.4 million cells. This is a low cell count, even for an "inviscid grid," for a complex model like the Elytron 4S UAV.

[††] When comparing CPUs and GPUs of "similar class," e.g., a desktop-class PC with low- to mid-end GPUs, or a workstation-class PC with high-end GPUs.

RotCFD Grid Setup

Since the Elytron 4S UAV model will be tested in low Reynolds number flight, it is assumed that the general domain size can be set to roughly 5 characteristic dimensions to the sides and upstream of the model, and 10 characteristic dimensions downstream of the model, to roughly approximate an unbounded medium. Both the upper and lower wing pair have a dihedral and sweep angle. The dihedral and sweep of the main wings require a high cell density, within an inherent Cartesian grid, to produce smooth airfoil cross sections—despite the tetrahedral near-body grid.

In RotCFD all grid sizing is relative to the grid size specified at the domain boundary. For each "refinement" of grid level in grid refinement regions, the grid size is essentially halved. The first objective was to find a gridding solution that was under 1.4 million cells and with an acceptable time step still ensuring stability of the simulation. Several stages in the gridding process are listed in Table 1. Every "refinement level" increase means the cell size for the Cartesian grid is divided by 2. In effect the cell size can be approximated by

$$ a_{rl} = \frac{A_{global}}{2^{[n_g - n_{rl}] - 1}} $$

Where $n_g = 4$ is the global refinement level, n_{rl} is the refinement level for which the cell size is to be approximated, and A_{global} is the dimension of a boundary or global cell.

Refinement level estimates were made for the main components of the aircraft: body, main wings, and vertical plates. The body was estimated to be refined between 9 and 11. The main wings were refined between 10 and 11, and the vertical plates at 11. The vertical plates were chosen to be gridded non-body fitted; this decision had a large influence on cell count and stability but was not expected to influence results, because they are not intended as lifting surfaces and are actually flat plates on the physical model. The cell count limit for running in OpenCL mode for the current GPUs ruled out the possibility of a full grid resolution study, as evidently the grid refinement should be higher in some areas.

Table 1. Grid study for the Elytron 4S UAV.

Grid Name	Body Refinement	Upper Wing Refinement	Lower Wing Refinement	Vertical Plate Refinement	Cell Count (10^6)	Comments
T1	9	10	10	N/A	0.50	
T2	10	11	10	N/A	2.00	GPU Limit
T3	9-11 (ABR)	9-11 (ABR)	9-11 (ABR)	N/A	1.40	
T4	9	10	11	11	1.50	GPU Limit
T5	10	10	10	11	1.10	
T6	9	10	10	11	1.30	
T7	9	10	10	11	1.31	Wake
T8	9	10	10	11	1.33	Wake

Both the model without the nose fan cutout (labeled "clean") and the model with the cutout (labeled "pow") were gridded. The unpowered, rotors-off runs were performed on the clean model, whereas the powered, rotors-on simulations were performed with the model including cutout—whether the nose fan was included or not. Some grid refinements use automated body refinement (ABR) where RotCFD itself refines the grid based on the CAD model gradients between user-specified refinement limits.

The time-step related stability criterion mostly dictates the required time step. This can be orders of magnitude smaller than what the Courant Friedrich Levy (CFL) condition dictates, likely suggesting some improvements in the program can still be made. For convergence of forces and rotor performance, the simulation time was initially set for the free-stream velocity to traverse the domain length twice. The residuals in that time will have converged but will show change upon the wake closing in on the downstream boundary condition. Time steps required can get excessive, and therefore a particular grid may not be feasible to solve within a reasonable wall clock time. Table 2 shows the approximate time-step requirements and corresponding run time (for the total time length) for the different cases given in Table 1.

Points of attention were the GDDR limits, refinement of the wake, near-body refinement, and rotor timing within the time step for an unsteady rotor model. Approximately 100,000 cells must be reserved for the front fan cutout later on. Figure 12 shows the refinement of the various critical areas. The cell count limit makes it hard to fully capture all surfaces smoothly despite the absence of a proper boundary layer grid (or viscous grid). Since a full grid resolution study is not within the scope of this effort, the objective is to see what, within the opposed cell count limit, is possible and how well trends can be captured under this limit. The final choice for a stable grid was grid T8 (see Table 3). An example of the grid showing the rotor wake region refinement is shown in Figure 12.

Table 2. Approximate time-step requirement for grid studies.

Name	Stable T/ts Ratio (s/ts)	Estimated Run Time (days)	Comments
T1	0.4/10,000	1	
T2	0.1/10,000	100	OpenMP
T3	0.1/10,000	40	
T4	N/A	N/A	OpenMP
T5	N/A	N/A	Not converging
T6	0.25/10,000	2.5	
T7	0.25/10,000	2.5	
T8	2.00/80,000	20	

Table 3. Initial and final refinement choices for grid T8.

Parameter	Description	Initial Refinement	Final Refinement
Global refinement	Smallest cell size	4	4
Wake refinement	First-level refinement of grid around body	4 - 8	7
Wake near body	Second-level refinement of grid around body	6 - 8	8
Body	Refinement of body components	6 - 8	9 - 10
Main rotor wash	Refinement in main rotor wake region	9	9
Fan wash	Refinement in fan wash region	10	10
Vertical plate refinement	Vertical plate unfitted refinement	11	11
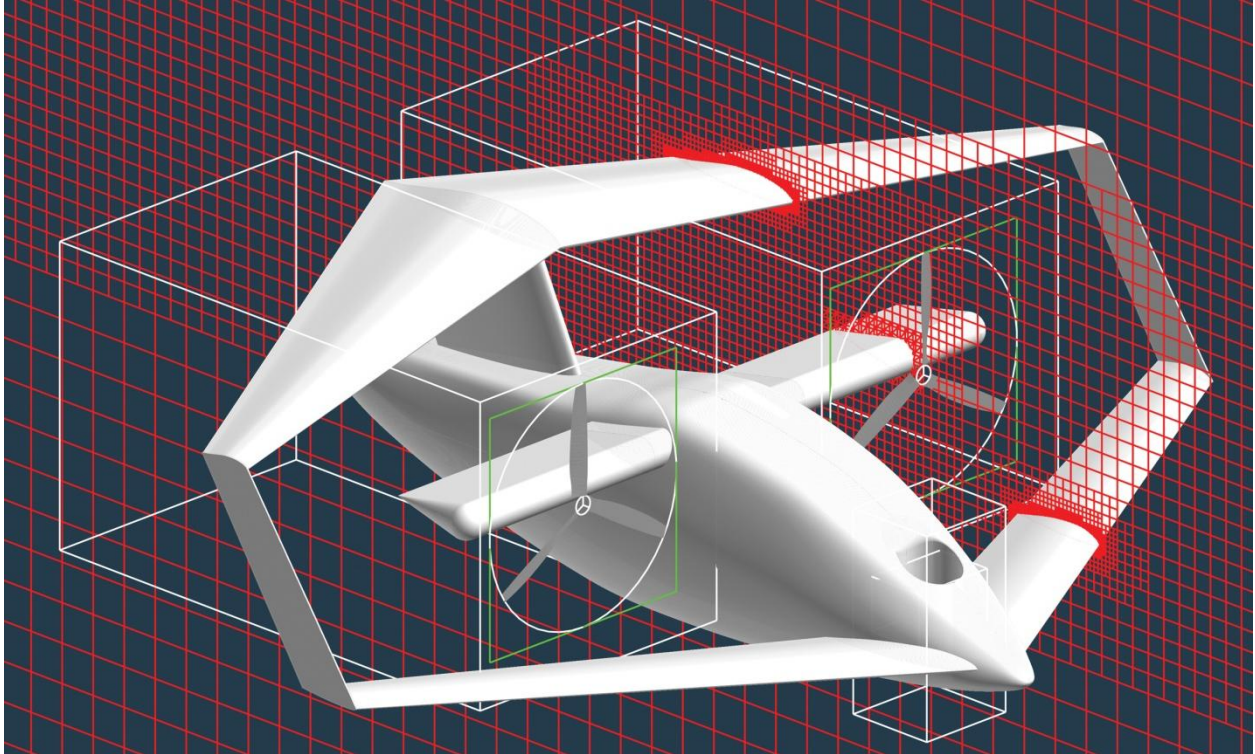
Figure 12. Elytron 4S UAV CAD model and gridding slice showing main rotor wake region (RotCFD).

Figure 13 and Figure 14 show the grid of the model. The global refinement, wake refinement, and wake near-body refinement gradually increase the flow-field refinement near the body in Figure 13. Figure 14 shows the body with the cutout with body refinement at level 10 over the cutout.
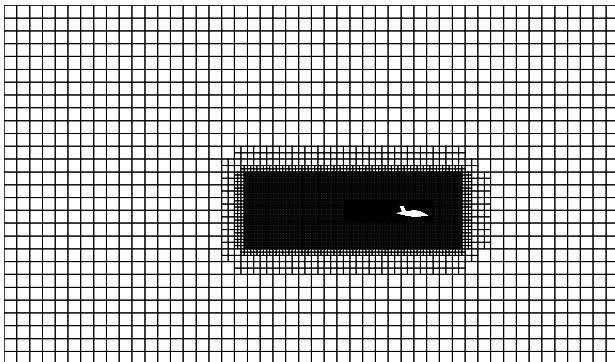
Figure 13. Flow-field domain in the *yz*-plane.
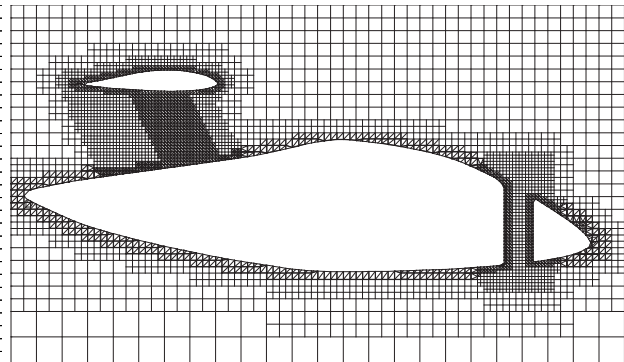
Figure 14. Near-body grid for the Elytron 4S UAV.

The Rotor Model

The main rotors used on the Elytron 4S UAV run at 9,000 RPM for VTOL. The nose fan operates at 37,000 RPM for VTOL mode. Both rotor and fans are fixed-pitched plastic models. To generate the airfoil tables, the rotors were measured using a Creaform MetraScan 70 3D optical laser scanner. Cross sections are normalized, and C81 tables are generated for a Mach number range varying RPM from 0 to 9000. The aerodynamic coefficients are obtained from XFOIL [4]. Appropriate Reynolds numbers per radial station (indicates Mach range) and RPM (based on Mach number) are inputted in XFOIL. Upon C81 generation, Reynolds number must be varied with Mach number range variation. The angles of attack examined are moderate to high (–20 to +20 degrees angle of attack), and the rest of the range (–180 to +180 degrees angle of attack) is populated with NACA 0012 experimental data because XFOIL is not adequate beyond stall. C81 files are generated for airfoils at r/R = 0.50, 0.75, and 0.95.

The main rotor thrust was trimmed to be almost equivalent to the drag observed at zero angle of attack and zero sideslip angle. This thrust setting (RPM control) was set the same for all cases. This constant RPM setting was deemed valid because of the small angles of attack and sideslip under consideration. Unsteady main rotor step size per time step was kept at 1.35 degrees per time step. For the grid chosen, there were around 24 cells over blade diameter and wake region. Table 4 shows the velocity, Mach, and Reynolds number ranges for the main rotor.

The nose fan was simulated using a similar approach, but no reference thrust values are available. The nose fan is only active in VTOL mode. Table 5 shows the simulated thrust values for the main rotors and nose fan, with and without tip correction applied in RotCFD. Tip corrections are implemented as a linear reduction of lift. Lift goes to zero at the tip over a specified region near the tip, usually between 0 to 5 percent blade span. For the present work, the tip correction was applied over the outboard 5 percent of the blade span. Correct modeling of the ducted fan was considered outside of the scope of the present research as the short aspect ratio blades and interaction with the duct likely require higher order modeling. The blade loading and aerodynamic coefficient distribution over the blade span were monitored and judged to be within normal operating ranges.

Table 4. Main rotor critical variable ranges.

Variable	Main Rotor Root		Main Rotor Tip	
	Cruise	VTOL	Cruise	VTOL
V (m/s)	63	78	135	167
M (-)	0.18	0.23	0.40	0.57
Re (-)	$8.81 \cdot 10^4$	$1.09 \cdot 10^5$	$1.42 \cdot 10^5$	$2.03 \cdot 10^5$

Table 5. Performance predictions for the isolated rotor and fan.

	Without Tip Correction		With Tip Correction	
	Thrust, T (N)	Thrust, T (lbf)	Thrust, T (N)	Thrust, T (lbf)
Main rotor	48.0	10.8	44.9	10.1
Nose fan	36.0	8.1	24.3	5.5

The main rotor thrust values correspond to the nominal thrust values as specified by the rotor manufacturer. The design thrust distribution in VTOL mode for the Elytron 4S UAV was 80–20 percent for the main rotors and fan, respectively. The rotor performance predictions indicate a 79–21 percent lift distribution.

Rotor Rotation Direction

The rotor/propeller slipstream increases the dynamic pressure over the tiltwing, therefore locally increasing the lift. The swirl of the main rotor causes a varying local angle-of-attack change and an asymmetric lift distribution. On one side the rotor counteracts the wing lift (rotor blade moving down) and the other side reinforces the lift (rotor blade moving upwards). This is more pronounced at low-speed, high-thrust settings.

Tip loss is observed through a local induced angle-of-attack change causing the lift near the tip to be reduced. While the typical design practice for tiltrotors is outboard-down in airplane mode [5], this does not hold for the Elytron 4S UAV design since the propeller is mounted in the center of the wing (and not on the tip).

By placing the rotor "outboard-up," part of the tip loss could be compensated by this asymmetric lift distribution through swirl (and perhaps the slipstream's increase in dynamic pressure as well). The velocity ranges of the aircraft, slipstream, and swirl need to be investigated before determining if this will have a significant effect, but it was considered best-practice to mount the main rotors outboard-up anyway.

Run Settings

RotUNS was run with 40,000 time steps per second for 2 seconds. Convergence was observed at roughly 30,000–40,000 time steps. Grid adaptation (both dynamic flow-field grid adaptation and static body grid adaptation) was not attempted.

All simulations were run with the realizable k-ε turbulence model with special wall function. All simulations were run time-accurate with unsteady rotor models (BEM). Velocity boundary conditions are applied on all surfaces resembling free-stream conditions, except for those that have a flow direction exiting the control volume. The body and grid are fixed, and the changes in angle of attack or sideslip angle are simulated by varying the velocity boundary condition components accordingly. The walls of the flow-field domain with exiting flow are modeled using the mass-outflow correction boundary condition. In the case of VTOL operation, the nose fan is modeled as an actuator disk (ADM) type instead of an unsteady rotor model to alleviate the time-step requirements at the nominal operating RPM of 37,000.

Test Matrix and Data Processing

The simulations are assumed to be at International Standard Atmosphere (ISA) and all units are according to the International System of Units (SI). The primary goal is to obtain data on a moderate angle of attack and sideslip sweep. Additional goals included tunnel interference tests and VTOL ground effect evaluation. All cases are simulated at a free-stream velocity of $V = 40\ kts$ as this was the estimated cruise velocity for the Elytron 4S UAV, and all tunnel tests were performed at the same velocity.

Angle-of-Attack and Sideslip Sweeps

The main sweeps are described in Table 6. An α of 0.0 degrees is not repeated for the beta sweeps as the case is identical to a β of 0.0 degrees. The β of -7.5-degree cases are run to identify possible grid issues not completely ensuring a symmetrical case. The grid for each case is identical as the boundary conditions are used to simulate the changes in flow angles. The unpowered sweeps are done with the fan cutout not present on the model. The powered sweeps have the cutout present, but no fan is modeled in the simulations. Thrust of rotors is manually trimmed to be slightly higher than expected drag to create a realistic cruise scenario.

VTOL Case in Ground Effect (IGE)

The VTOL case IGE was simulated with the body at a height from the ground expected when the landing gear is present. The T8 grid was used but with an unfitted grid. This was done to allow for a longer simulation time to observe the wake behavior of the flow where the flow over the body was not of prime importance for aerodynamic quantities. The simulation comprises 10 seconds at 108,000 time steps to show global flow in ground effect. The alpha sweep is described in Table 7.

For stability and geometry avoidance, the nose fan diameter was reduced from r/R = 0.043 m to 0.042 m. The fan was modeled using an ADM instead of a BEM for simulation stability reasons at its very high RPM and proximity to geometry.

Tunnel Interference Cases

To investigate tunnel interference effects several cases were simulated in the U.S. Army 7- by 10-Foot Wind Tunnel test section, modeled as a constant area duct (see Table 8). The grid of the angle-of-attack and sideslip sweeps was cropped to match the tunnel test section length. Grid refinement along the walls was increased, and the wall boundary condition was set to viscous wall. The flow-field domain was elongated to ensure that no interference from the inlet boundary condition altered the flow conditions at the body.

Table 6. Alpha and beta sweep case details.

Case	Main Rotors	Nose Fan	Cutout in Geometry	Alpha (deg)	Beta (deg)
Alpha sweep				0.0, 2.5, 5.0, 7.5, and 10.0	0.0
Beta sweeps				0.0	2.5, 5.0, 7.5, 10.0, and -7.5
Powered alpha sweep	●		●	0.0, 2.5, 5.0, 7.5, and 10.0	0.0
Powered beta sweep	●		●	0.0	2.5, 5.0, 7.5, 10.0, and -7.5

Table 7. VTOL case details.

Case	Main Rotors	Nose Fan	Cutout in Geometry	Alpha (deg)	Beta (deg)
Alpha sweep	●	●	●	0.0	0.0

Table 8. 7- by 10-foot tunnel case details.

Case	Main Rotors	Nose Fan	Cutout in Geometry	Alpha (deg)	Beta (deg)
Empty tunnel				0.0	0.0
7- by 10-ft with body			●	0.0	0.0
7- by 10-ft with powered body	●		●	0.0	0.0

Processing of Output Values

The rotor model only interacts with the body through the rotor wake as the rotor forces and moments are not included in the integrated (body) forces output from RotCFD. The thrust is added to the results in the post-processing phase. Forces and moments resolved around the origin of the model, in the symmetry plane intersection with the tiltwing tilt axis (which coincides with the tiltwing quarter-chord location). Forces and moments on the body in RotCFD were transformed from body axis to wind axis system. Rotor thrust, torque, and power values were also recorded. The sign definitions used in the simulations are shown in Table 9.

At the time of simulation, the final Center of Gravity (CG) was not determined. For the moment calculation, the definition of the geometric offset of the CG from the CAD model origin is described in Table 10. The CAD origin is the intersection of the quarter-chord location of the tiltwing and the *xz*-symmetry plane.

Table 9. Sign definitions used in simulations.

Quantity	Positive Direction
x	Body-fixed, "upstream"
y	Body-fixed right, looking forward
z	Body-fixed, "down"
Lift, L	"Up," normal to freestream
Drag, D	Downstream, parallel to freestream
Side force, S	Right, looking forward
Roll, ϕ	Right wing down
Pitch, θ	Nose up
Yaw, ψ	Nose right
Angle of attack, α	Nose up
Angle of sideslip, β	Nose left "wind from the right"

Table 10. Definition of variable CG location in reference to CAD origin.

Variable	Cartesian Axis	Description	Distance (m)
a	z (positive down)	Distance of new CG location from origin	0.0057
b	x (positive forward)	Distance of new CG location from origin	0.0500
c	y (positive out of right wing)	Distance between origin and rotor thrust vector	0.3240

The calculation of the forces, including the thrust vectors for the alpha sweep, is performed as:

$$\begin{vmatrix} F_D \\ F_S \\ F_L \end{vmatrix} = \begin{bmatrix} -\cos\alpha & 0 & -\sin\alpha \\ 0 & 1 & 0 \\ \sin\alpha & 0 & -\cos\alpha \end{bmatrix} \begin{vmatrix} F_{x_b} \\ F_{y_b} \\ F_{z_b} \end{vmatrix} + \begin{bmatrix} -\cos\alpha & 0 & 0 \\ 0 & 0 & 0 \\ \sin\alpha & 0 & 0 \end{bmatrix} \begin{vmatrix} F_{T_R} + F_{T_L} \\ 0 \\ 0 \end{vmatrix}$$

where F_D, F_S, and F_L are the drag, side force, and lift force, respectively. F_{x_b}, F_{y_b}, and F_{z_b} are the body forces in the body axis system. F_{T_R} and F_{T_L} are the thrust force for the right and left rotor, respectively, looking upstream. The calculation of the forces, including the thrust vectors for the beta sweep, is performed as

$$\begin{vmatrix} F_D \\ F_S \\ F_L \end{vmatrix} = \begin{bmatrix} -\cos\beta & -\sin\beta & 0 \\ -\sin\beta & \cos\beta & 0 \\ 0 & 0 & -1 \end{bmatrix} \begin{vmatrix} F_{x_b} \\ F_{y_b} \\ F_{z_b} \end{vmatrix} + \begin{bmatrix} -\cos\beta & 0 & 0 \\ -\sin\beta & 0 & 0 \\ 0 & 0 & 0 \end{bmatrix} \begin{vmatrix} F_{T_R} + F_{T_L} \\ 0 \\ 0 \end{vmatrix}$$

The calculation of the moments, including the thrust vectors and body forces, is performed as

$$\begin{vmatrix} M_x \\ M_y \\ M_z \end{vmatrix} = \begin{vmatrix} M_{x_b} \\ M_{y_b} \\ M_{z_b} \end{vmatrix} + \begin{bmatrix} 0 & a & 0 \\ -a & 0 & b \\ 0 & -b & 0 \end{bmatrix} \begin{vmatrix} F_{x_b} \\ F_{y_b} \\ F_{z_b} \end{vmatrix} + \begin{bmatrix} 0 & 0 & 0 \\ -a & 0 & 0 \\ c & 0 & 0 \end{bmatrix} \begin{vmatrix} F_{T_L} \\ 0 \\ 0 \end{vmatrix} + \begin{bmatrix} 0 & 0 & 0 \\ -a & 0 & 0 \\ -c & 0 & 0 \end{bmatrix} \begin{vmatrix} F_{T_R} \\ 0 \\ 0 \end{vmatrix} + \begin{vmatrix} M_{Q_R} + M_{Q_L} \\ 0 \\ 0 \end{vmatrix}$$

where M_x, M_y, and M_z are the total moments on the body. M_{x_b}, M_{y_b}, and M_{z_b} are the moments due to the aerodynamic forces on the body. M_{Q_R} and M_{Q_L} are the torque values of the right and left rotor, respectively. The (roll) moment on the aircraft due to the motor torque was insignificant because of the counter-rotating propellers and is effectively ignored. The contributions of the rotor drag and side force, and hub moments are assumed to be negligible as they were found to be several orders smaller than the corresponding contributions from the rotor thrust and torque, and body forces and moments.

Data Processing

RotCFD outputs body forces on body only, so the rotor thrust is obtained separately from the rotor model, but the rotor wake effect on the body is present. The left- and right-half of the wings and fuselage are monitored independently to allow for in-depth analysis of the separate components.

The force and moments on the Elytron 4S UAV components displayed slight oscillatory convergence. Therefore, the arithmetic mean, μ, of the required variables over the converged solutions range was taken as the performance metric. The data extremes and standard deviations were extracted simultaneously but proved to be mostly insignificant at the corresponding magnitudes of the variables.

Convergence of residuals, forces, and rotor performance were monitored to ensure converged solutions.

Wind Tunnel Testing: U.S. Army 7- by 10-Foot Wind Tunnel

The Elytron 4S UAV was tested in the U.S. Army 7- by 10-Foot Wind Tunnel at NASA Ames as part of a larger test program early in 2017. The goal of the test program was to characterize the aerodynamic performance of a number of small multirotor unmanned aircraft systems.

To measure the performance of the Elytron 4S UAV, the model was mounted on a "sting stand" as shown in Figure 15. The orientation of the model was fixed. Yaw could be adjusted during run time using the tunnel turntable. Pitch was adjusted manually using the pitch mechanism shown in Figure 16. Because changing the pitch was a manual process, only a handful of pitch angles were tested. These values were representative of the pitch angles that would be encountered by the vehicle in free flight. Vertical position of the model could be adjusted slightly by turning a jack screw under the horizontal arm of the sting stand in order to bring the model closer to the tunnel centerline.

The experimental technique largely followed that of Russell et al. [6], which gives a more complete description of the model control and data acquisition methodology. Aerodynamic loads were measured in a body-fixed frame of reference, with the x-, y-, and z-directions defined positive aft, right, and up, respectively. Moments in the x-, y, and z-directions were defined positive roll right, nose up, and nose right, respectively. The loads were measured using a JR3 100-lb six-axis load cell, which can measure maximum loads of 100 lb in the x- and y-directions, 200 lb in the z-direction, and 300 in-lb in all three moment axes. Manufacturer stated accuracy of the load cell is 0.25 percent of full-scale, but Russell et al. [6] found that, in practice, the measurement uncertainty was less than this value.

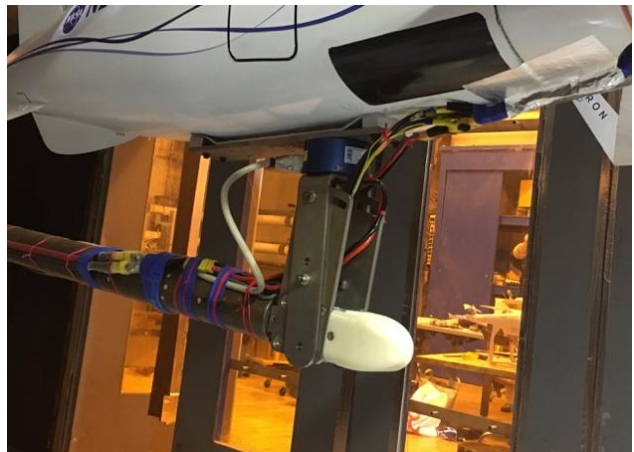**Figure 15. Elytron 4S UAV installed in the U.S. Army 7- by 10-Foot Wind Tunnel.**

Figure 16. Close-up of the Elytron 4S UAV model mounting hardware.

Motor/rotor speed was controlled using a Pololu[‡‡] Mini Maestro servo controller, with RPM measurements from Eagle Tree[§§] brushless motor RPM sensors. The deflection angles of the flaps on the two wings, as well as the tilt angle of the center wing, could also be controlled remotely through the servo controller. In addition to the force and moment measurements of the load cell, voltage and current to the motors was measured, so electrical power of the two motors could be calculated.

The two flight regimes of interest during the test were low-speed transition and the lower end of the cruise configuration speed range. Table 11 gives a summary of the test matrix. The Elytron 4S UAV was tested both with and without the rotors installed. For the runs without the rotors installed, the cutout for the nose fan was taped over, so air could not flow through it. A single run, listed at the end of Table 11, was performed with the rotors uninstalled and the tape removed.

The data were post-processed to convert the load cell voltages into engineering units (lb and in-lb). In addition, corrections were made for load cell temperature drift as well as wake and solid body tunnel blockage. No aerodynamic tares were applied. The support structure above the load cell for the 4S UAV was very minimal, so the omission of aero tares did not introduce significant measurement errors.

Table 11. Elytron 4S UAV wind tunnel test matrix.

Pitch (deg)	Yaw (deg)	Speed (ft/s)	Rotor RPM	Center Wing Tilt (deg)	Elevator Deflection (deg)	Configuration
0.0	-10.0 to 7.5	67	5,800 to 7,200	0	0	Full vehicle
2.5	-5.0 to 2.5	67	5,800 to 7,200	0	0	Full vehicle
7.5	-5.0 to 2.5	67	5,800 to 7,200	0	0	Full vehicle
10.0	-5.0 to 0.0	67	5,800 to 7,200	0	0	Full vehicle
2.5	0.0	40	6,500 and 7,200	0, 15, 25	-20, 0, 25	Full vehicle
2.5	0.0	20	6,500 and 7,200	0, 15, 25, 45	0	Full vehicle
5.0	0.0	40	6,500 and 7,200	0, 15, 25	-20, 0, 25	Full vehicle
5.0	0.0	20	6,500 and 7,200	0, 15, 25, 45	-20, 0, 25	Full vehicle
7.5	0.0	40	6,500 and 7,200	0, 15, 25	-20, 0, 25	Full vehicle
7.5	0.0	20	6,500 and 7,200	0, 15, 25, 45	-20, 0, 25	Full vehicle
0.0	-10.0 to 10.0	67	n/a	0	0	Rotors off
2.5	-5.0 to 2.5	67	n/a	0	0	Rotors off
5.0	-5.0 to 2.5	67	n/a	0	0	Rotors off
7.5	-5.0 to 2.5	67	n/a	0	0	Rotors off
10.0	-5.0 to 2.5	67	n/a	0	0	Rotors off
5.0	-5.0 to 2.5	67	n/a	0	0	Rotors off, no tape

[‡‡] https://www.pololu.com/
[§§] http://www.eagletreesystems.com/

Results

The following sections present the comparison between the RotCFD simulations at $V = 40\ kts$ and experimental values for the "clean" (no rotors, no nose cutout) and "full" (rotors, nose cutout) configurations (see Table 6). Both an angle-of-attack sweep and an angle-of-sideslip sweep are performed. The aircraft is not in trim for both the experiments and simulations. All experimental values are fully corrected for tunnel effects and are indicated using the "EXP" notation. Simulation results for the U.S. Army's 7- by 10-foot test section size are performed for zero angle of attack and angle of sideslip to observe the simulated influence of the walls and are labeled "7x10." All forces and moments are presented as the arithmetic means over the converged results (e.g., μF_L or μM_x).

Tunnel Interference Cases

The tunnel interference cases (see Table 8) are provided to show the estimated tunnel interference and its rough magnitude. Tunnel simulations are highly complicated and only corrected experimental results are presented. No comparison is made with uncorrected experimental results as the tunnels are simulated as constant-area ducts, and proper treatment of the flow conditions is beyond the scope of the present research.

Rotors Off: Angle-of-Attack Sweep

Figure 17, Figure 18, and Figure 19 show the comparison between the RotCFD simulations and the experimental lift, drag, and side forces, respectively. All angle-of-attack sweeps are performed at $\beta = 0.0$ degree.

The lift curve slope is near-identical, albeit with an offset in angle of attack of around 2 degrees. The offset was measured to be around 2 degrees during tunnel testing but was not corrected for, as the exact number was unknown because there was no available reference line on the aircraft.
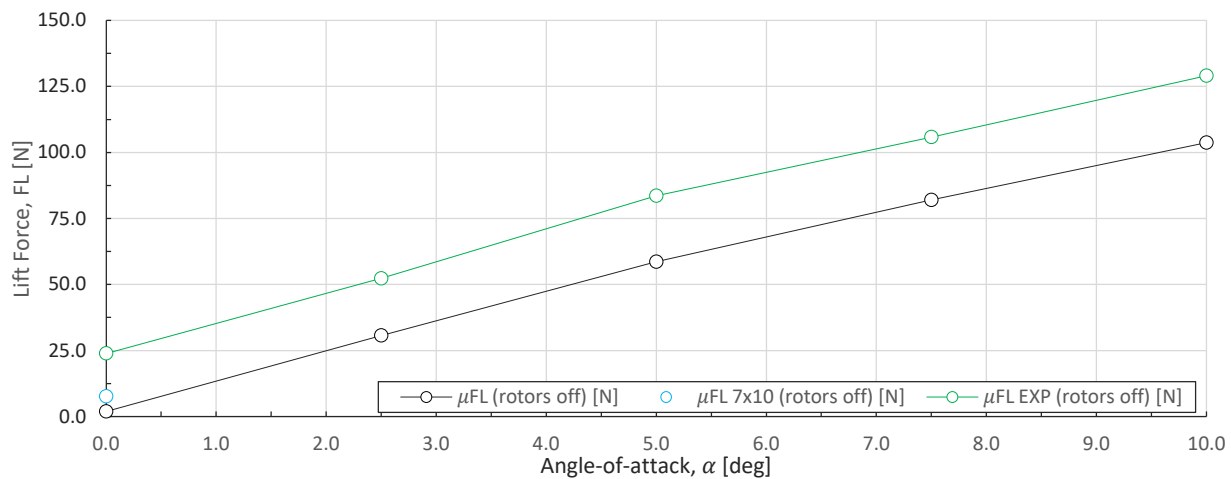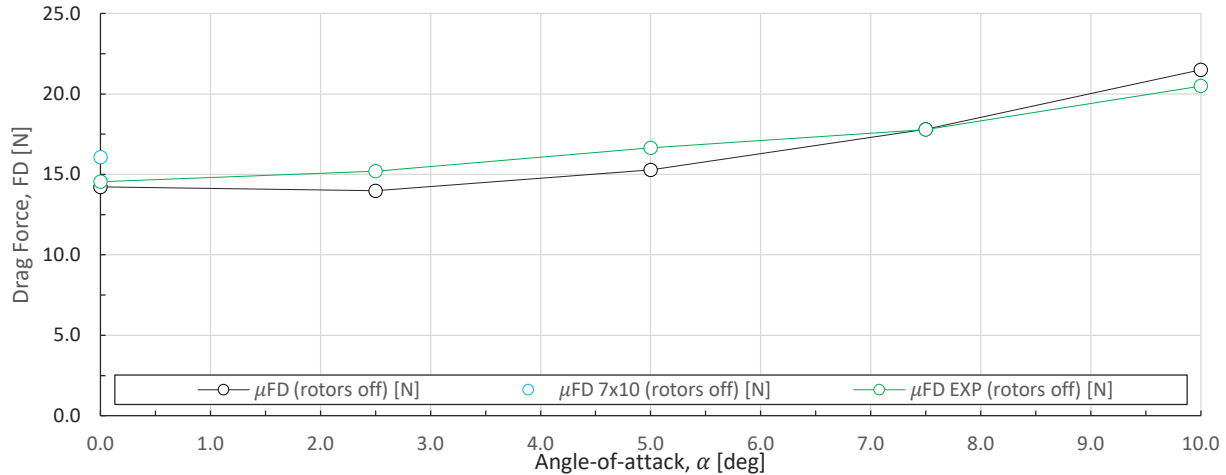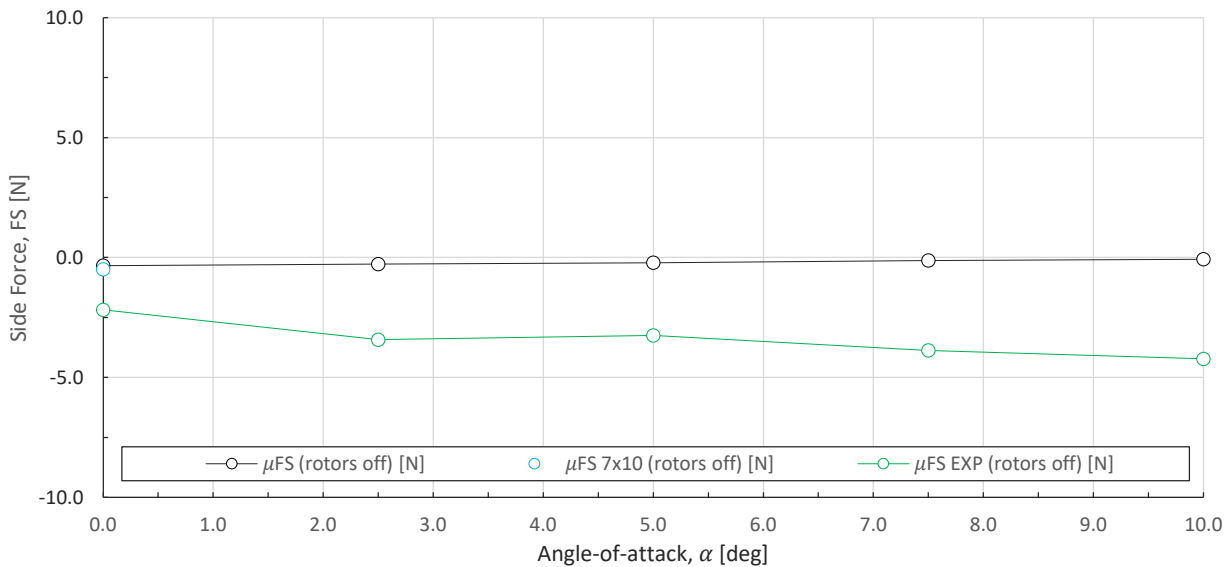

Figure 17. Rotors-off lift force for angle-of-attack sweep variation.

Figure 18. Rotors-off drag force for angle-of-attack sweep variation.

Figure 19. Rotors-off side force for angle-of-attack sweep variation.

The drag predictions are adequate, especially considering the relatively coarse mesh used. The pressure drag is expected to dominate because of the bluff fuselage shape. The dependency of the correct drag prediction on the correct simulation of the friction drag component by the turbulence model (and wall function) is then hypothesized to be partially negated by the large pressure drag component due to the bluff fuselage shape.

The simulated side force shows a near-constant offset that is attributed to tunnel misalignment and/or manufacturing errors. The CAD model is fully symmetric in the *xz*-plane, but small gridding inconsistencies cause minor side force asymmetry.

Figure 20, Figure 21, and Figure 22 show the comparison between the RotCFD simulations and the experimental pitch, roll, and yaw moments, respectively. The label "CG" is added when the simulations moment reference point has been transformed to reflect the CG adjustment to match the tunnel model.

The data indicate the aircraft is stable in the tested angle-of-attack range, but the simulated sensitivity to a change in angle of attack is not really pronounced. The experiment shows an inflexion point in the pitch sensitivity after 7.5 degrees angle of attack, resulting in a positive slope.

Comparison of the roll moments shows a near-constant offset, hypothesized to originate from tunnel misalignment and/or manufacturing errors. As said before, the CAD model is fully symmetric. The value is near zero as expected.

Comparison of the yaw moments shows a near-constant offset, attributed to tunnel misalignment and/or manufacturing errors. The value is near zero as expected.
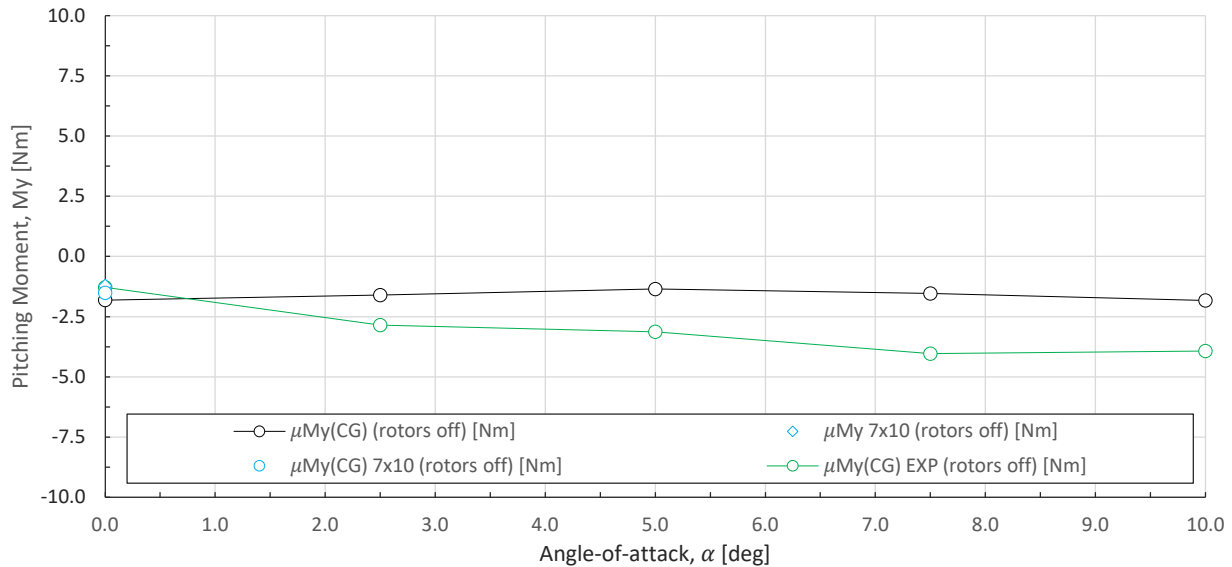
Figure 20. Rotors-off pitching moment for angle-of-attack sweep variation.
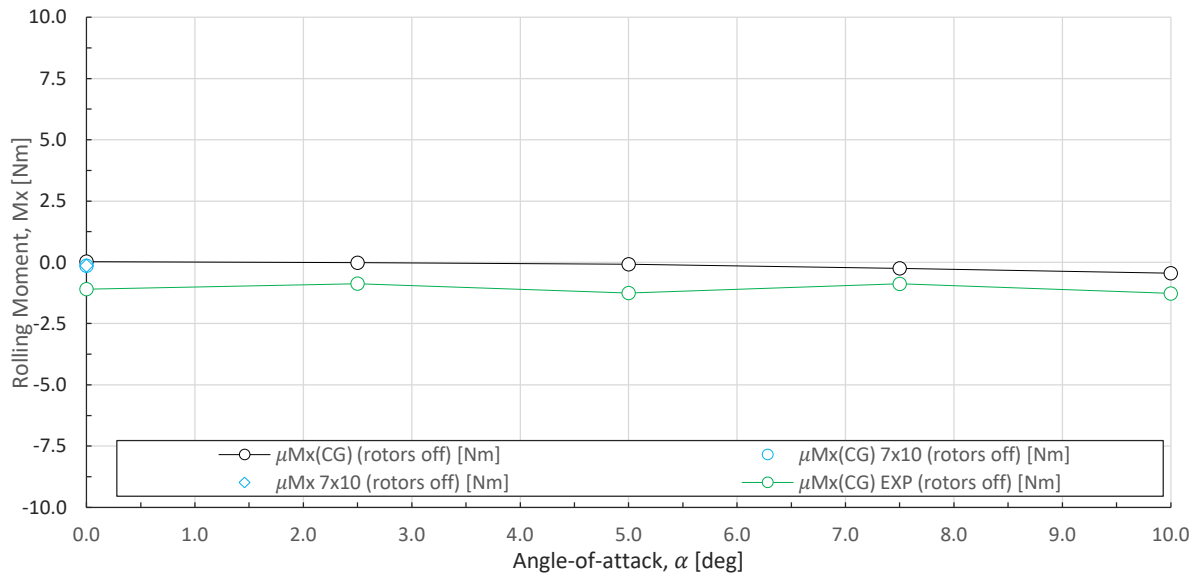
**Figure 21. Rotors-off rolling moment for angle-of-attack sweep variation.**

19
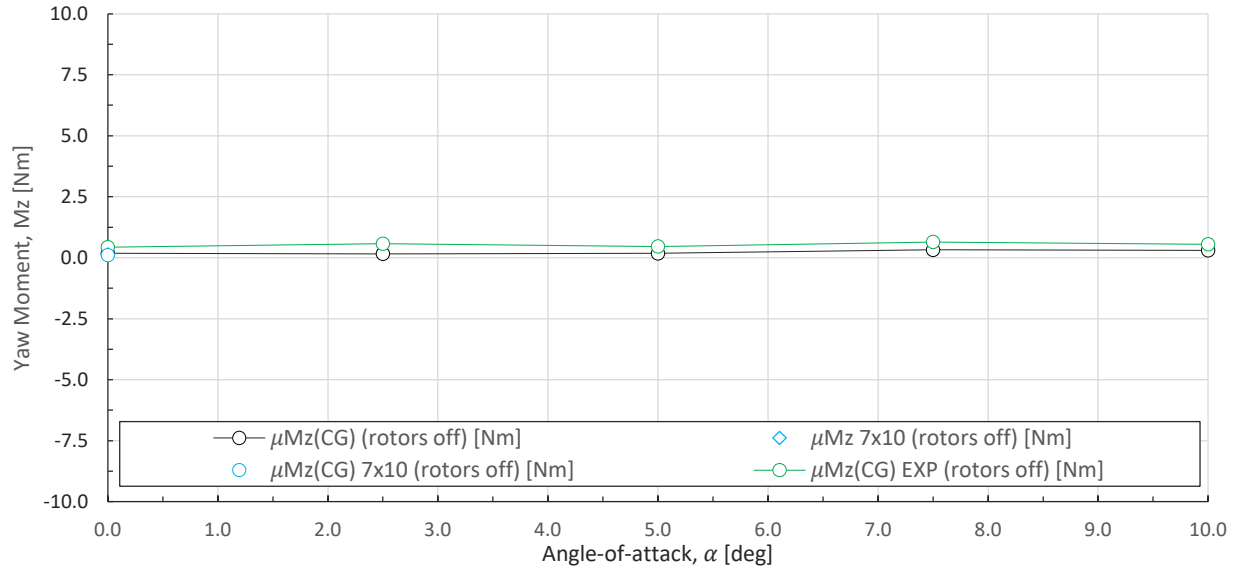
**Figure 22. Rotors-off yaw moment for angle-of-attack sweep variation.**

Rotors Off: Angle-of-Sideslip Sweep

The following section shows the results of the angle-of-sideslip sweep for the rotors-off configuration. Because of the lift offset at zero angle-of-attack, the lift forces are expected to show a near-constant offset of the same magnitude as observed in Figure 17. The simulations are only performed for positive angles of sideslip (because of symmetry), except for one control point simulation at $\beta = -7.5$ degrees.
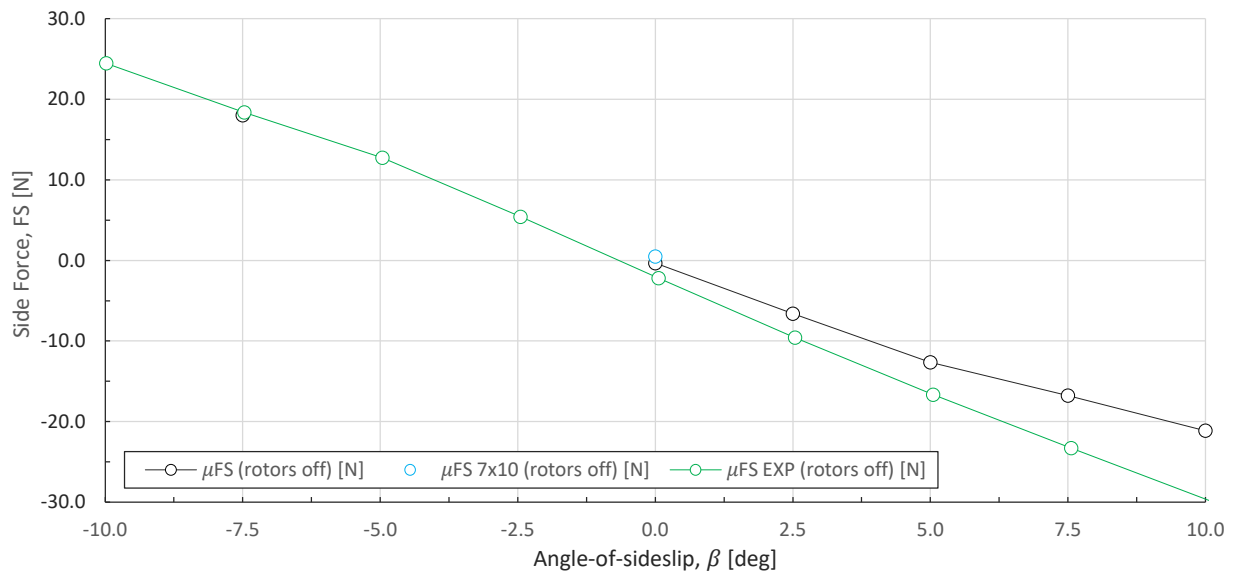
Figure 23, Figure 24, and Figure 25 show the comparison between the RotCFD simulations and the experimental lift, drag, and side forces, respectively. All angle-of-sideslip sweeps are performed at $\alpha = 0.0$ degrees.
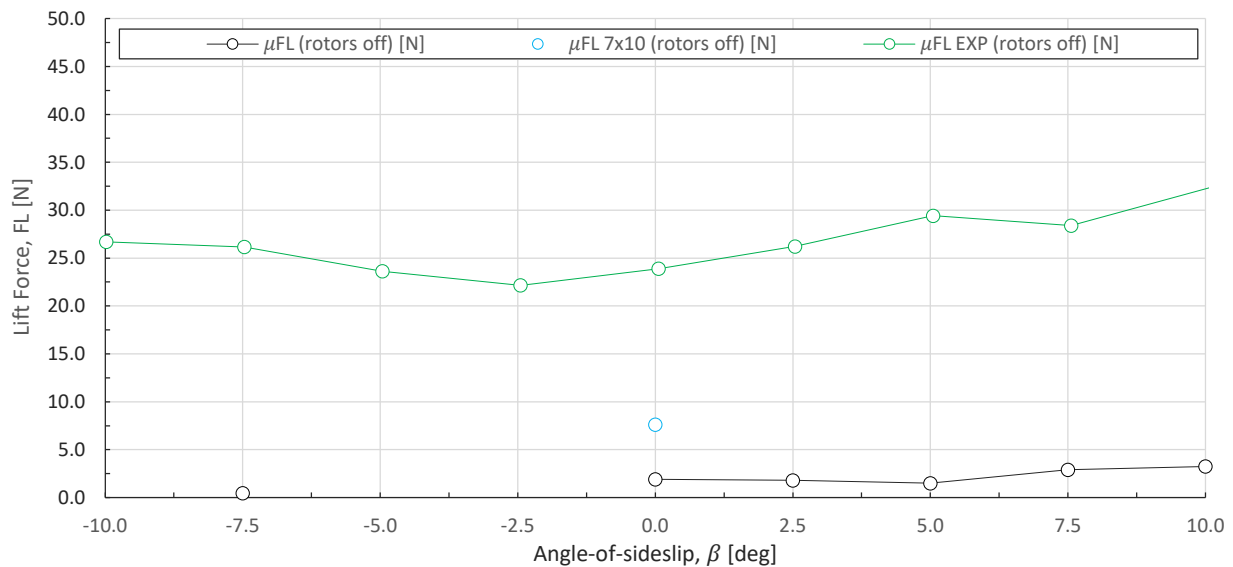
Figure 23. Rotors-off lift force for sideslip sweep variation.

20
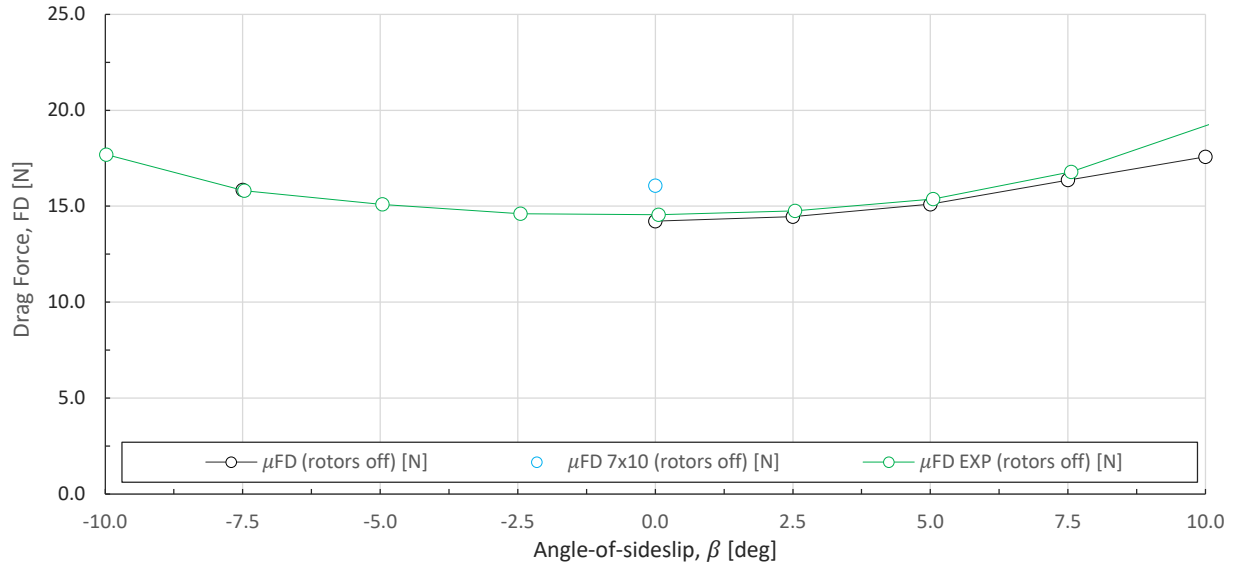
**Figure 24. Rotors-off drag force for sideslip sweep variation.**

Figure 25. Rotors-off side force for sideslip sweep variation.

The lift force results show the same offset in lift as observed in Figure 17. The experimental results suggest a slight offset of the model to the freestream of around 2.5 degrees.

The drag comparison is adequate, expected to originate from the large pressure drag component. In excess of $\alpha = 7.5$ degrees, it is likely the onset of stall will start to deteriorate the CFD simulations.

The side force shows a fair comparison of the slope. Figure 26, Figure 27, and Figure 28 show the comparison between the RotCFD simulations and the experimental pitch, roll, and yaw moments, respectively. The label "CG" is added when the simulations moment reference point has been transformed to reflect the CG adjustment to match the tunnel model.

Both the simulated rolling and pitching moment sensitivity to sideslip are not really pronounced when compared to the experimental results and no conclusions are drawn.
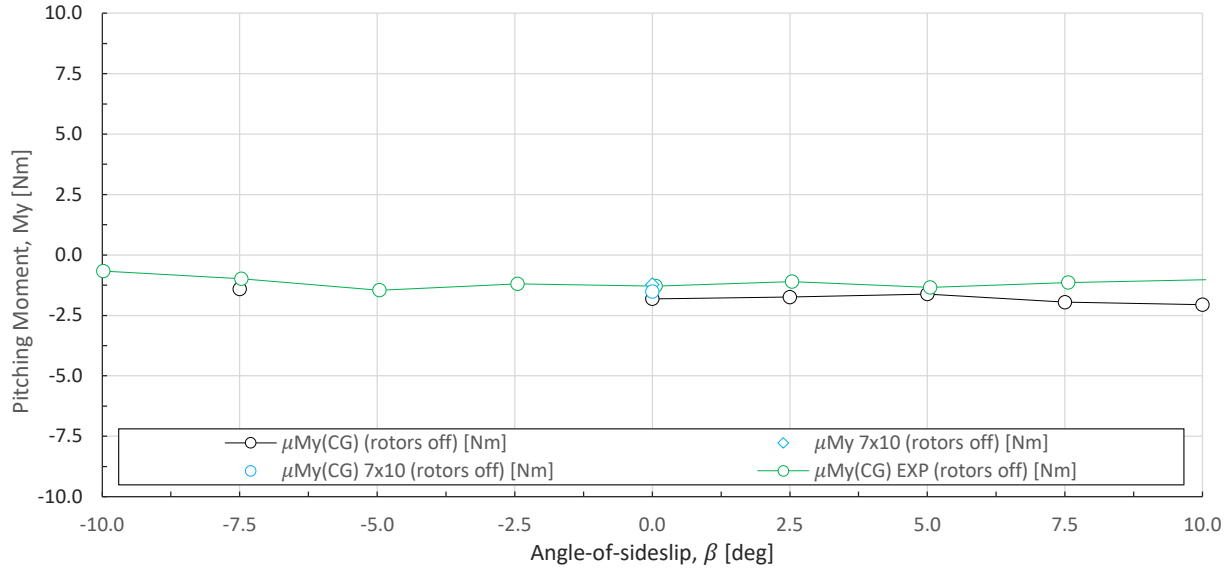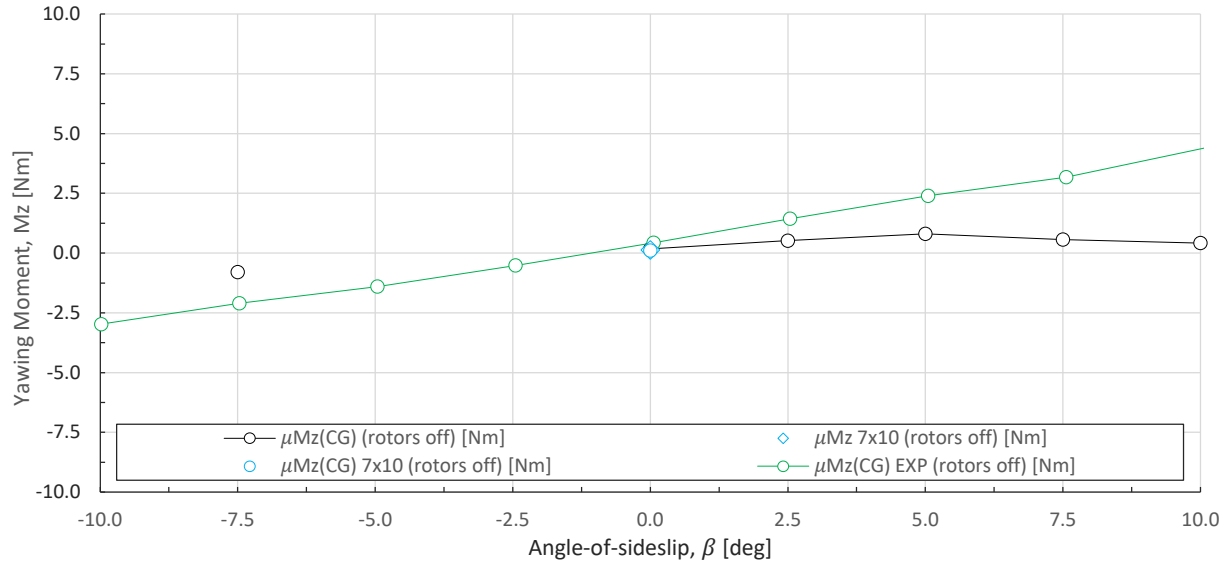

Figure 26. Rotors-off pitching moment for sideslip sweep variation.
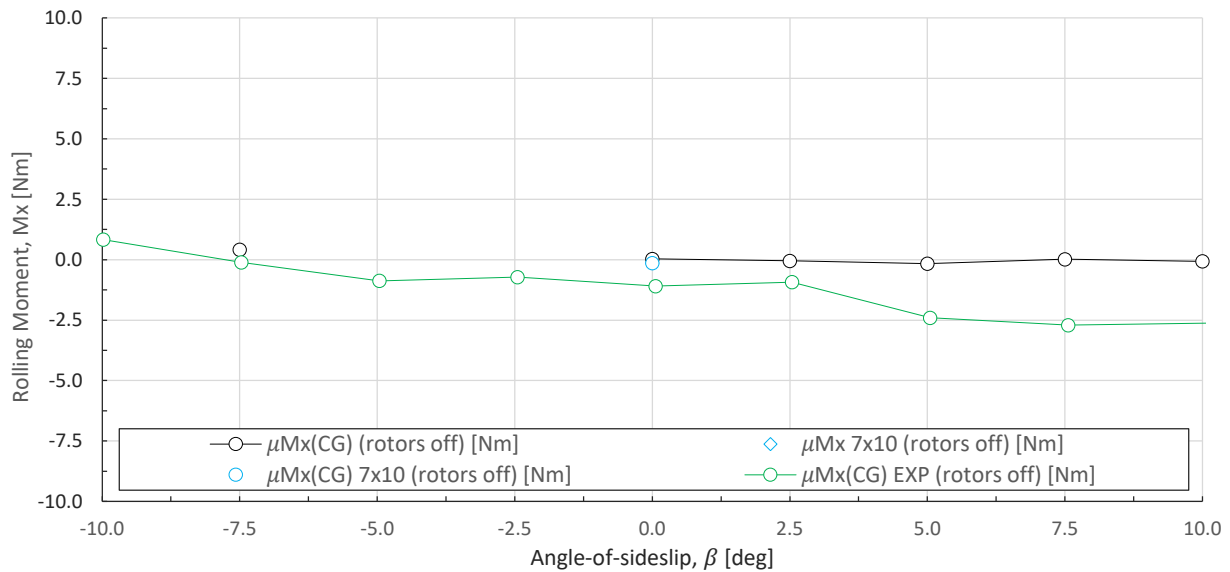
Figure 27. Rotors-off rolling moment for sideslip sweep variation.

Figure 28. Rotors-off yaw moment for sideslip sweep variation.

The simulation does not reveal a sensitivity of the yaw moment to the sideslip angle. The experimental model had increased rudder size and two ventral fins, showing higher directional stability of the model in the experiment. The increased rudder size and addition of the ventral fins was not simulated, which is assumed to explain the stability differences between the simulated and experimental data.
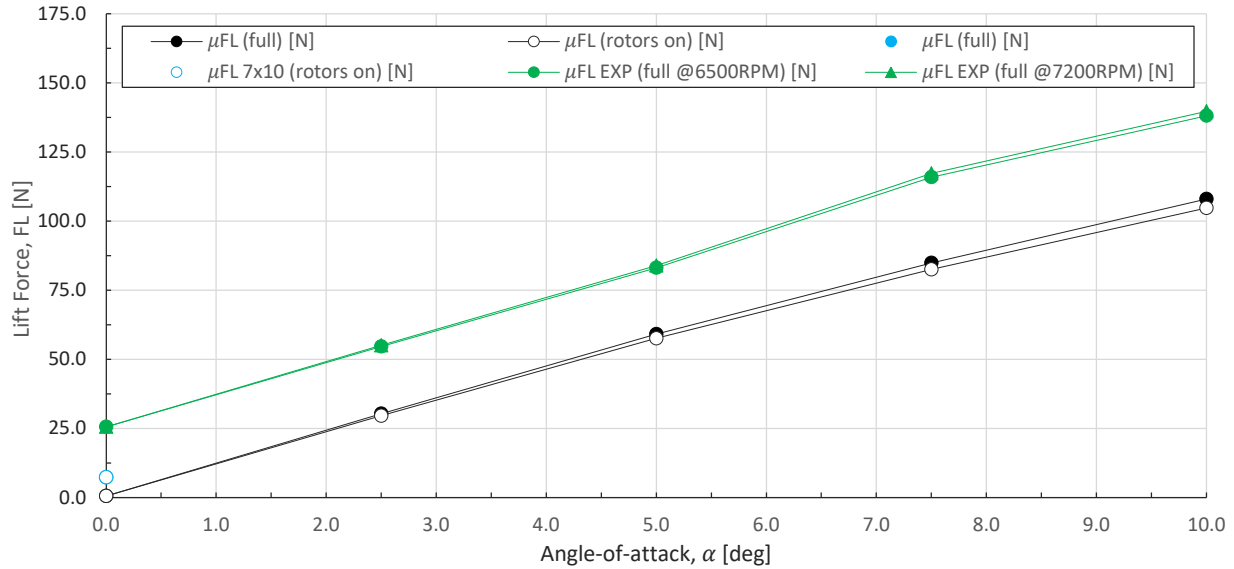
Full Vehicle: Angle-of-Attack Sweep

Figure 29, Figure 30, and Figure 31 show the comparison between the RotCFD simulations and the experimental lift, drag, and side forces, respectively. All angle-of-attack sweeps are performed at $\beta = 0.0$ degrees. The simulations with the designation "full" indicate the full vehicle with rotor forces and moments. Simulations with the designation "rotors on" do not have the rotor forces and moments added up to the total forces and moments presented, but the rotor wake is, however, experienced by the fuselage. This is possible because RotCFD outputs integrated body forces and moments separate from rotor forces and moments.

Similar to the rotors-off configuration, the lift curve slope is near-identical, albeit with an offset in angle of attack of around 2 degrees. The change between 6,500 and 7,200 RPM in the experiments shows negligible differences for the lift force. The difference between the "rotors-on" and "full" simulations is insignificant, again, simply indicating the minor contribution of the rotor thrust to lift.

Similar to the rotors-off configuration in Figure 18, the comparison in drag for the full configuration is adequate. Again, the dependency of the correct drag prediction on the correct simulation of the friction drag component by the turbulence model is partially negated by the large pressure drag component. The experimental rotor diameter was increased, and therefore, for equal RPM, a higher thrust is expected. The simulated rotor was set to 7,200 RPM; the tunnel model predicts an estimated 6,800 RPM with simulation, in line with the expectations. The

(simulated) rotors-on drag magnitude increased compared to the rotors-off configuration in Figure 18 because of the rotor wake inclusion on the integrated forces.
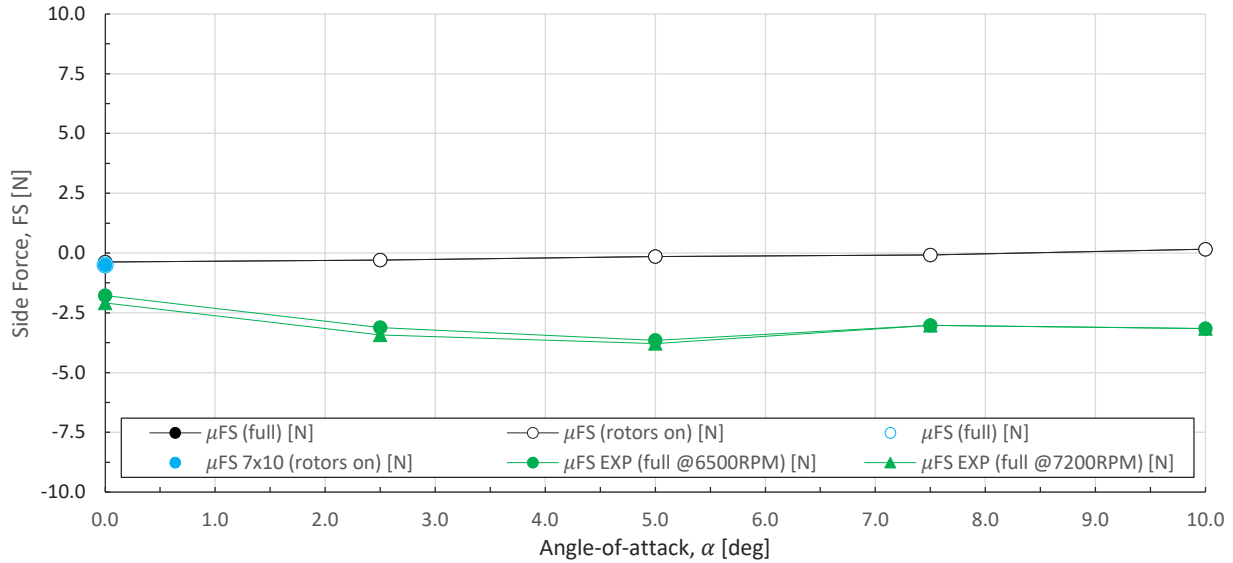
The side force shows a near-constant offset that is attributed to tunnel misalignment and/or manufacturing errors. The CAD model is fully symmetric in the *xz*-plane.

**Figure 29. Full-vehicle lift force for angle-of-attack sweep variation.**
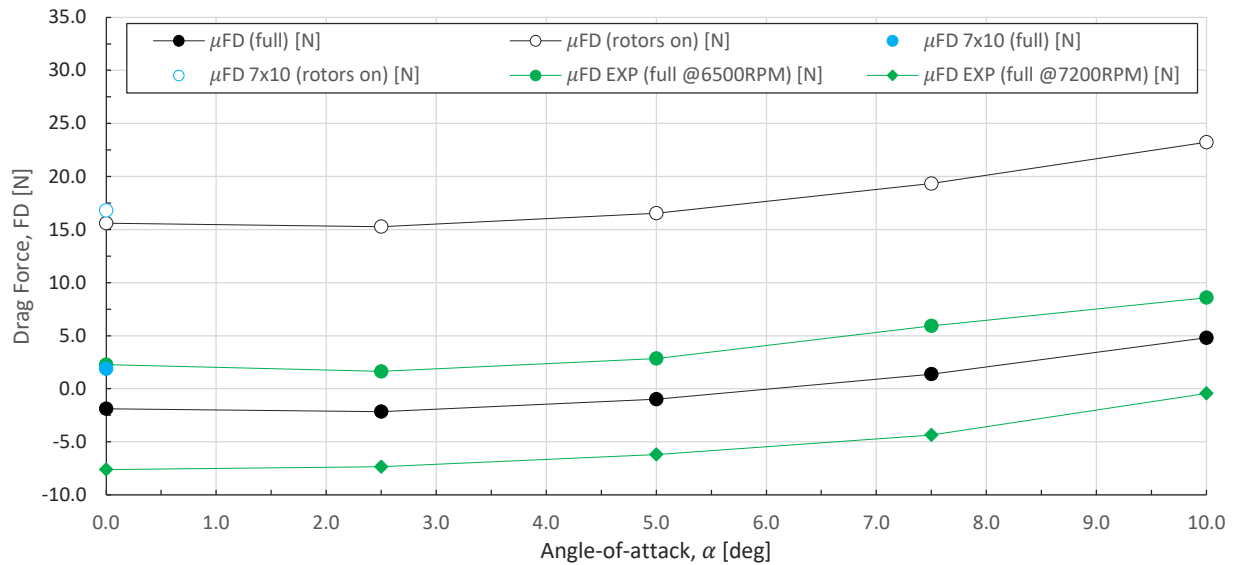
Figure 30. Full-vehicle drag force for angle-of-attack sweep variation.

24

Figure 31. Full-vehicle side force for angle-of-attack sweep variation.

Figure 32, Figure 33, and Figure 34 show the comparison between the RotCFD simulations and the experimental pitch, roll, and yaw moments, respectively. The label "CG" is added when the simulations moment reference point has been transformed to reflect the CG adjustment to match the tunnel model.

The simulated sensitivity to a change in angle of attack is not really pronounced when compared to the average magnitude of the experimental results. The pitching moment curves are shifted in the positive direction because of the rotor wake inclusion when compared to the rotors-off pitching moment variation in Figure 20.
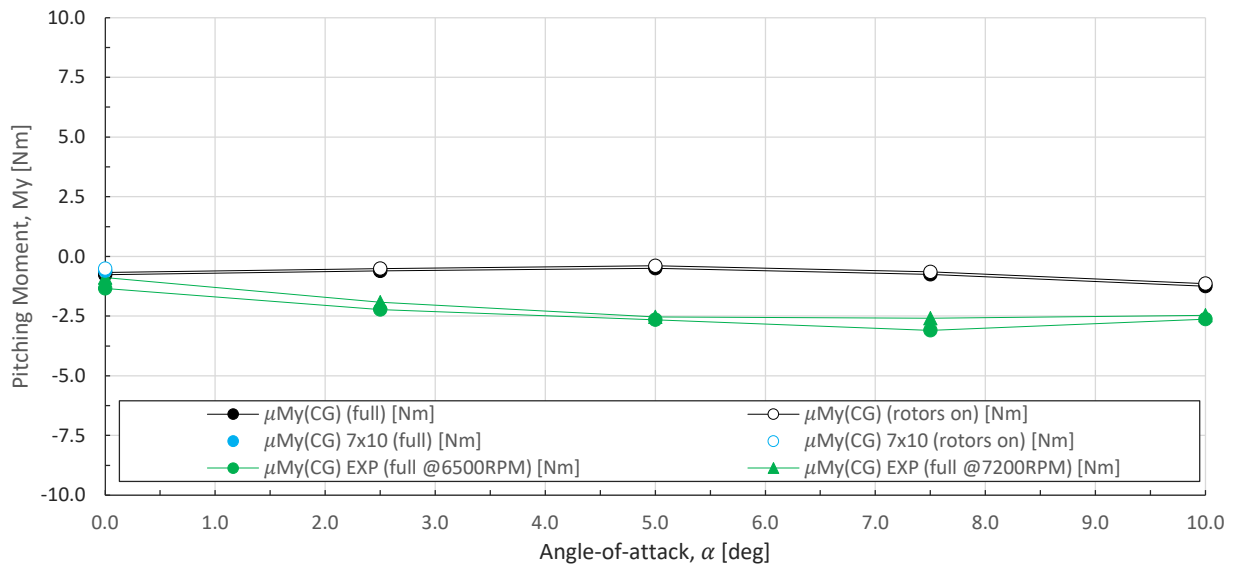
Figure 32. Full-vehicle pitching moment for angle-of-attack sweep variation.

25
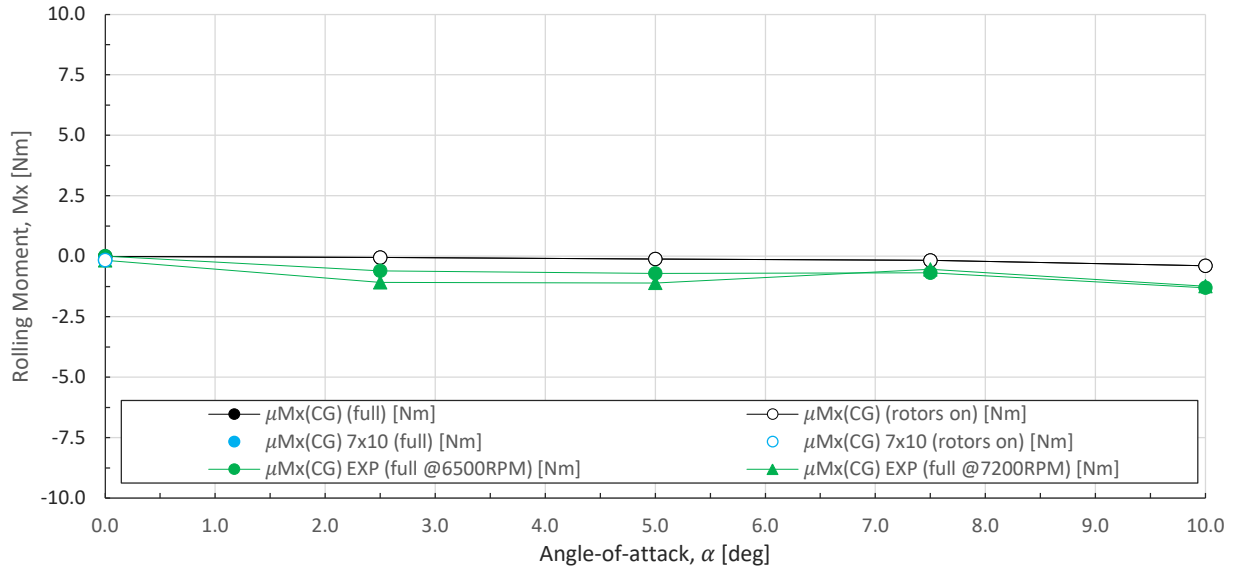
Figure 33. Full-vehicle rolling moment for angle-of-attack sweep variation.
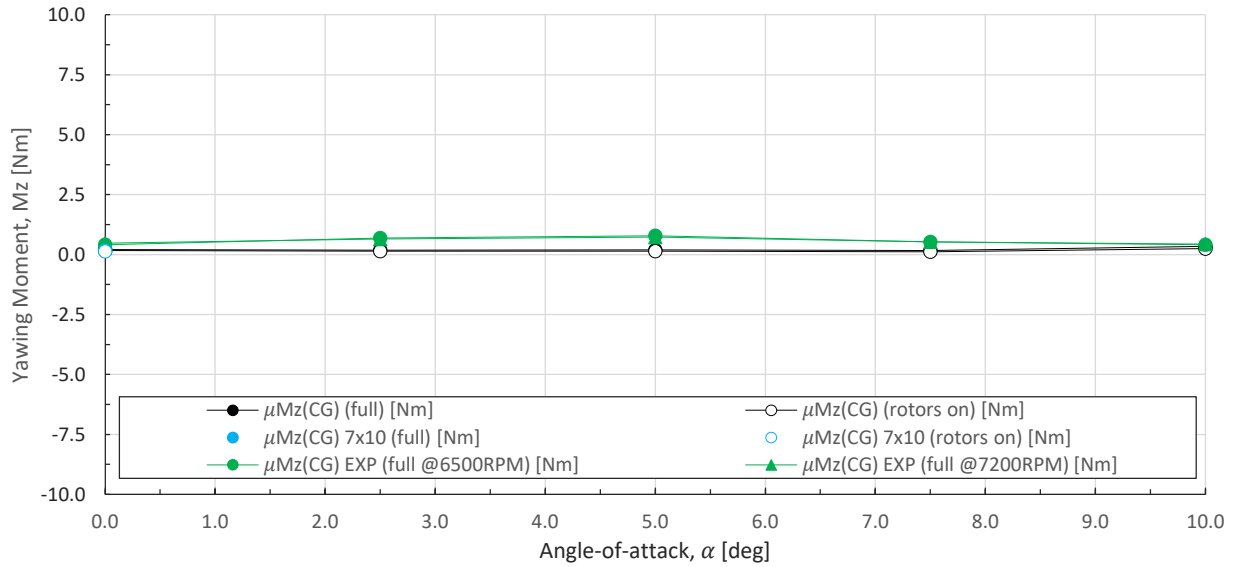
Figure 34. Full-vehicle yawing moment for angle-of-attack sweep variation.

The roll moment near-constant offset is likely attributable to tunnel misalignment and manufacturing errors. The magnitude of the simulated rolling moment sensitivity due to pitch is small in comparison to the magnitude of the observed experimental results. The small sensitivity to pitch can be a desirable quality as it indicates reduced cross coupling.

Both the simulated yawing and simulated rolling moment sensitivity to pitch seem insignificant compared to experimental results. For the sweep, no significant effects of propeller wash are identified.

Full Vehicle: Angle-of-Sideslip Sweeps

The following section shows the results of the angle-of-sideslip sweep for the full vehicle configuration. Because of the lift offset at zero angle of attack, the lift forces are expected to show a near-constant offset of the same magnitude as observed in Figure 17. The simulations are only performed for positive angles of sideslip (because of symmetry), except for one control simulation at $\beta = -7.5$ degrees as a control data point.

Figure 35, Figure 36, and Figure 37 show the comparison between the RotCFD simulations and the experimental lift, drag, and side forces, respectively. All angle-of-sideslip sweeps are performed at $\alpha = 0.0$ degrees. The simulations with designation "full" indicate the full vehicle with rotor forces and moments. Simulations with designation "rotors on" do not have the rotor forces and moments added up to the total forces and moments presented, but the rotor wake is, however, experienced by the fuselage. This is possible because RotCFD outputs integrated body forces and moments separate from rotor forces and moments.

The lift force results show the same offset in lift as observed in Figure 17. The experimental and simulation results both show slight differences in lift between $\beta = -7.5$ and $+7.5$ degrees. In the simulation this is attributed to differences in the grid, despite the symmetric source CAD model. The asymmetry observed in the experimental results is hypothesized to originate from a slight bank angle of the model during testing.

The experimental rotor diameter was increased, and therefore, for equal RPM, a higher thrust is expected. The simulated rotor was set to 7,200 RPM; the tunnel model predicts an estimated 6,800 RPM with simulation, in line with the expectations. The (simulated) rotors-on drag magnitude increased compared to the rotors-off configuration in Figure 24 because of the rotor wake inclusion on the integrated forces.
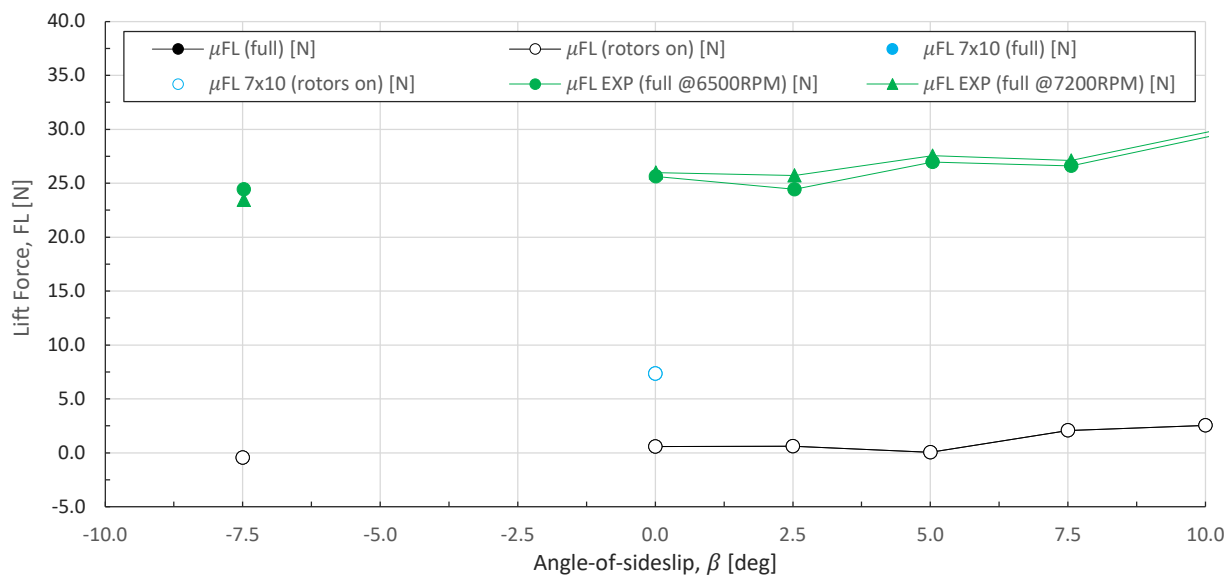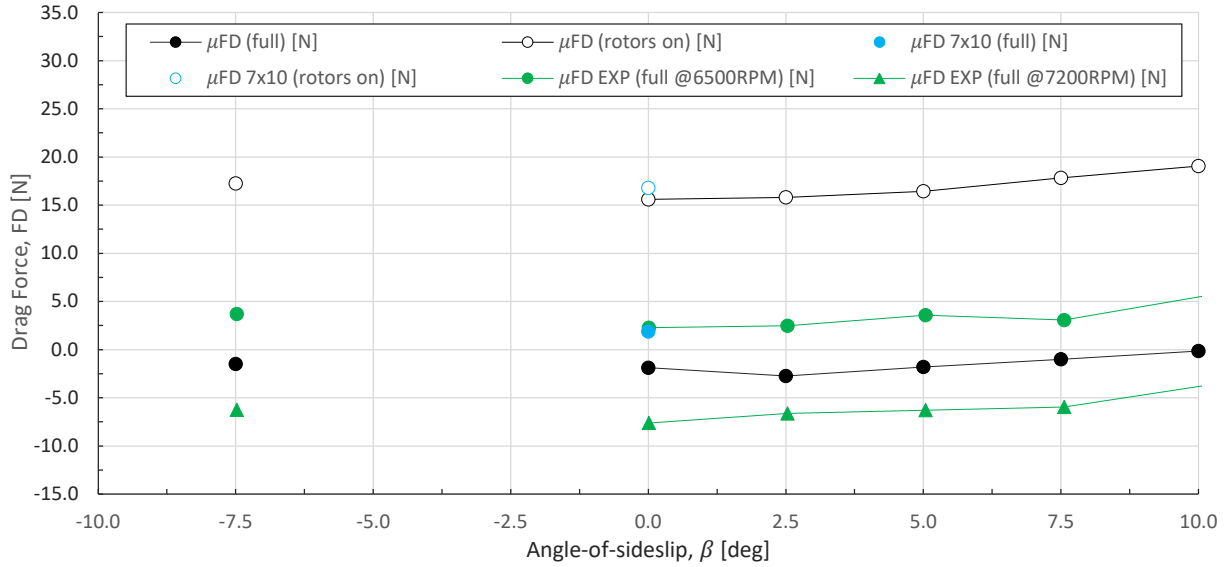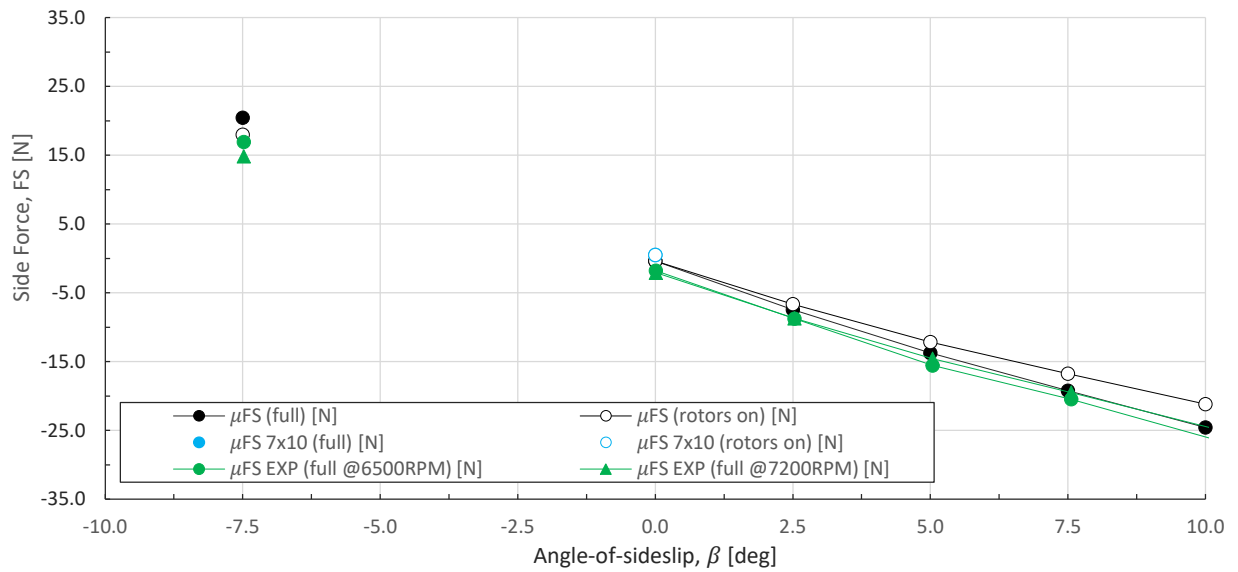

Figure 35. Full-vehicle lift force for sideslip sweep variation.

**Figure 36. Full-vehicle drag force for sideslip sweep variation.**

Figure 37. Full-vehicle side force for sideslip sweep variation.

The side force shows a fair comparison of the slope. Figure 38, Figure 39, and Figure 40 show the comparison between the RotCFD simulations and the experimental pitch, roll, and yaw moments, respectively. The label "CG" is added when the simulations moment reference point has been transformed to reflect the CG adjustment to match the tunnel model.

The rotors-on pitching moment curves are shifted in the positive direction because of the rotor wake inclusion when compared to the rotors-off pitching moment variation in Figure 26.

28

The tunnel picks up the sensitivity of the rolling moment because of sideslip, which is not noticed by RotCFD model.

The simulation does not reveal a sensitivity of the yaw moment to the sideslip angle. The experimental model had increased rudder size and two ventral fins, showing higher directional stability of the model in the experiment. The increased rudder size and addition of the ventral fins was not simulated, which is assumed to explain the stability differences between the simulated and experimental data.
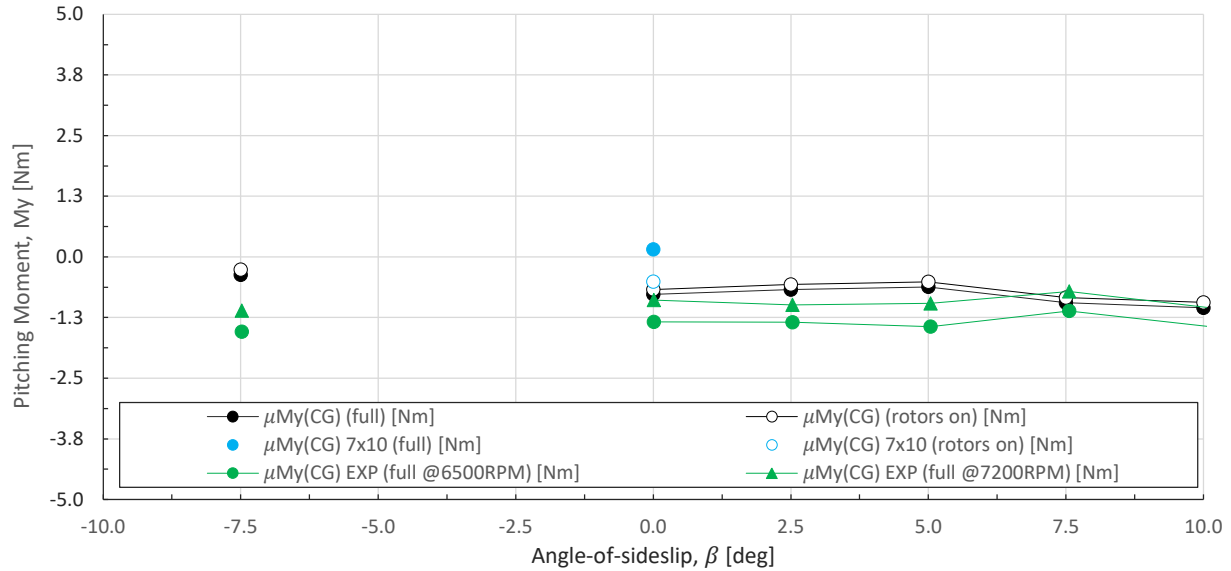
Figure 38. Full-vehicle pitching moment for sideslip sweep variation.
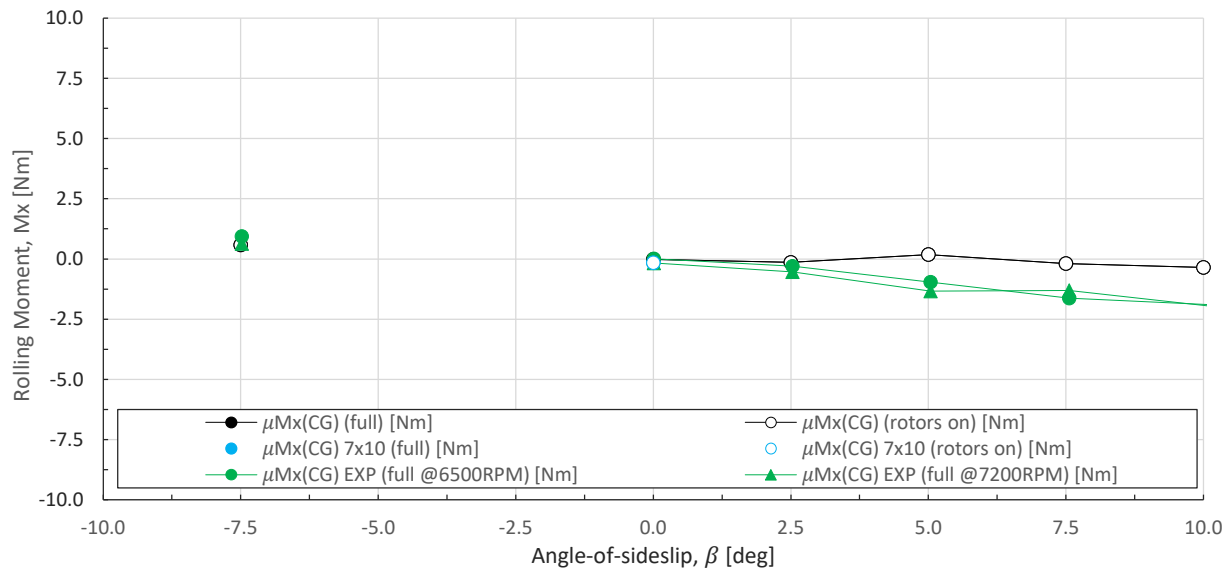
**Figure 39. Full-vehicle rolling moment for sideslip sweep variation.**
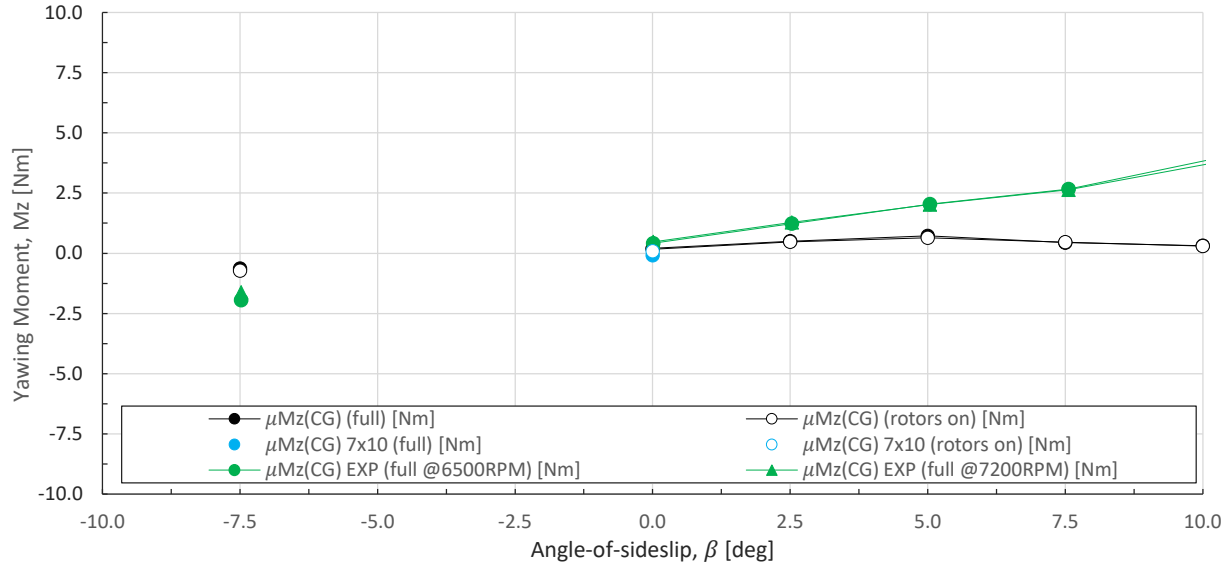
Figure 40. Full-vehicle yawing moment for sideslip sweep variation.

Full Vehicle: In Ground Effect (IGE)

Smoke studies were performed to investigate possible re-ingestion of the wake when operating IGE. The tests proved troublesome as the smoke would diffuse before it could be tracked to study its potential re-ingestion of the wake. Wake re-ingestion can cause foreign object debris (FOD) to create safety hazards by causing potential damage to the airframe, propellers, or engines. Figure 41 shows a snapshot at T = 0.25 s of the wake propagation visualized as various velocity magnitude iso-surfaces. This allows first-order studies in the wake behavior of the Elytron 4S UAV IGE. A small part of the tip vortices is resolved as vorticity iso-surface and can be seen trailing behind the main rotors. The wake of the nose fan is seen to propagate faster than the main rotors as the thrust-to-disk-area ratio is higher for the ducted fan. Both ducted fan and main rotor wakes spread out when they are near the ground plane and have reached a near steady-state solution. Overall it is expected that no clear re-ingestion of the wake occurs because of the presence of the ground plane and/or body.

30
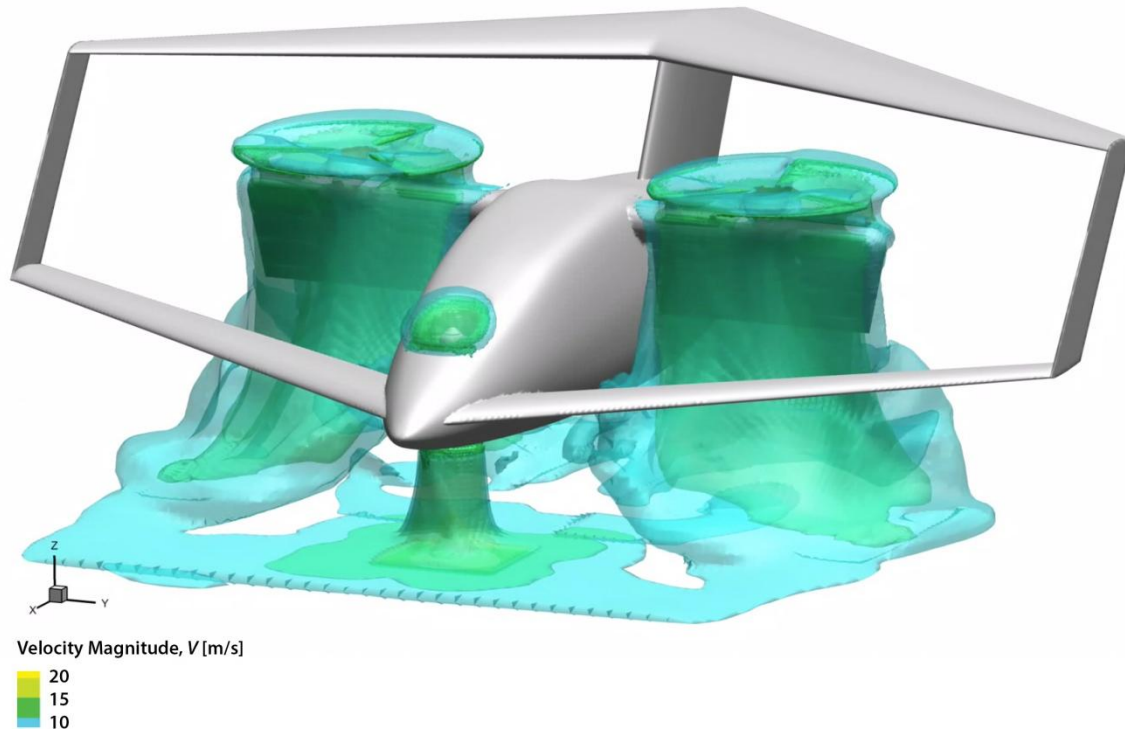
Figure 41. Velocity magnitude iso-surfaces to study wake behavior IGE.

Conclusions

The results and comparison with experiments show the promise of RotCFD as a tool for design with modern-day quick turnaround times. Based on these results, the following conclusions can be drawn:

- The results for the lift, drag, and side force are promising considering the mid-fidelity method employed.
- Clear differences in directional stability were observed. The effect of the increased rudder size and added ventral fins are hypothesized to cause the sensitivity to sideslip.
- The effect of the rotor diameter increase in the experiments is assumed to cause the differences in total net thrust/drag forces.
- Differences in the rotors-off versus rotors-on cases show influence of the rotor wake on pitching moment magnitude for both angle-of-attack and angle-of-sideslip sweeps.
- Simulated changes in airframe drag are also observed because of the effect of the rotor wake inclusion on the body for rotors-on cases.

Advances in GPU computing within RotCFD during the writing of this report have shown speed increases for equal simulations of around six times using more adequate GPUs. Also increased VRAM on those GPUs have allowed cell counts of up to 8 million. Mesh generation is almost automated, and execution of the code is cheap compared to supercomputing efforts for high-fidelity approaches.

References

[1]   Rajagopalan, R. G., Baskaran, V., Hollingsworth, A., Lestari, A., Garrick, D., Solis, E., and Hagerty, B., "RotCFD - A Tool for Aerodynamic Interference of Rotors: Validation and Capabilities," *American Helicopter Society International – Future Vertical Lift Aircraft Design Conference 2012*, San Francisco, CA, Jan. 18–20, 2012, pp. 311–327.

[2]   Koning, W. J. F., Acree, C. W., and Rajagopalan, G., "Using RotCFD to Predict Isolated XV-15 Rotor Performance," *American Helicopter Society International – AHS Specialists' Conference on Aeromechanics Design for Vertical Lift*, San Francisco, CA, Jan. 20–22, 2016.

[3]   Young, L. A., Yamauchi, G. K., and Rajagopalan, G., "Simulated Rotor Wake Interactions Resulting from Civil Tiltrotor Aircraft Operations Near Vertiport Terminals," *51st AIAA Aerospace Sciences Meeting including the New Horizons Forum and Aerospace Exposition*, Grapevine, TX, 2013.

[4]   Drela, M., "XFOIL: An Analysis and Design System for Low Reynolds Number Airfoils," *Low-Reynolds Number Aerodynamics*, 1989.

[5]   Yeo, H. and Johnson, W., "Performance and Design Investigation of Heavy Lift Tilt-Rotor with Aerodynamic Interference Effects," *Journal of Aircraft*, vol. 46, no. 4, 2009, pp. 1231–1239.

[6]   Russell, C., Willink, G., Theodore, C., Jung, J., and Glasner, B., "Wind Tunnel and Hover Performance Test Results for Multicopter UAS Vehicles," NASA/TM-2018-219758, 2018.